

Equilibrium Model Constraints on Baryon Cycling Across Cosmic Time

Sourav Mitra^{1*}, Romeel Davé^{1,2,3,4}, Kristian Finlator⁵

¹ *University of the Western Cape, Bellville, Cape Town 7535, South Africa*

² *South African Astronomical Observatories, Observatory, Cape Town 7925, South Africa*

³ *African Institute for Mathematical Sciences, Muizenberg, Cape Town 7945, South Africa*

⁴ *Astronomy Department, University of Arizona, Tucson, AZ 85721, USA*

⁵ *DARK fellow, Dark Cosmology Centre, Niels Bohr Institute, University of Copenhagen*

3 October 2018

ABSTRACT

Galaxies strongly self-regulate their growth via energetic feedback from stars, supernovae, and black holes, but these processes are among the least understood aspects of galaxy formation theory. We present an analytic galaxy evolution model that directly constrains such feedback processes from observed galaxy scaling relations. The equilibrium model, which is broadly valid for star-forming central galaxies that dominate cosmic star formation, is based on the ansatz that galaxies live in a slowly-evolving equilibrium between inflows, outflows, and star formation. Using a Bayesian Monte Carlo Markov chain approach, we constrain our model to match observed galaxy scaling relations between stellar mass and halo mass, star formation rate, and metallicity from $0 < z < 2$. A good fit ($\chi^2 \approx 1.6$) is achieved with eight free parameters. We further show that constraining our model to any two of the three data sets also produces a fit to the third that is within reasonable systematic uncertainties. The resulting best-fit parameters that describe baryon cycling suggest galactic outflow scalings intermediate between energy and momentum-driven winds, a weak dependence of wind recycling time on mass, and a quenching mass scale that evolves modestly upwards with redshift. This model further predicts a stellar mass-star formation rate relation that is in good agreement with observations to $z \sim 6$. Our results suggest that this simple analytic framework captures the basic physical processes required to model the mean evolution of stars and metals in galaxies, despite not incorporating many canonical ingredients of galaxy formation models such as merging or disk formation.

Key words: galaxies: formation, galaxies: evolution, galaxies: abundances, galaxies: mass function

1 INTRODUCTION

The formation and evolution of galaxies is governed by a vast number of interrelated physical processes that span many decades in physical and temporal scale. Such complexity makes this area of astrophysics extraordinarily rich and interesting, driven by the accelerating pace of observational data that has statistically characterised the multi-wavelength properties of galaxies from locally out to high redshifts. Yet, this physical complexity and wealth of data has proved to be an increasingly difficult challenge for models of galaxy formation, whose primary goal is to sort out which processes are responsible for which observables, and thereby elucidate the physics that drives galaxy evolution.

Currently, there are two main approaches to modeling galaxy formation: semi-analytic models (SAMs) and hydrodynamic simulations. SAMs are rooted in the classical analytic approaches of the 1970’s (Rees & Ostriker 1977; Binney 1977; White & Rees 1978), which posit that galaxies form as central baryonic condensations cooled from the virial temperature within dark matter halos, conserving angular momentum to form a disk (Fall & Efstathiou 1980; Dalcanton et al. 1997; Mo et al. 1998). With the emergence of the hierarchical cold dark matter (CDM) paradigm (Blumenthal et al. 1984), such disks followed the merging of dark matter halos via “merger trees” to build the observed galaxy population (White & Frenk 1991; Kauffmann et al. 1993; Somerville & Primack 1999). As the galaxy population became characterised with greater accuracy over a wider range of epochs, numerous free parameters were layered

* E-mail: hisourav@gmail.com

upon this framework in order to reproduce various observed galaxy properties, with these free parameters constrained by additional, putatively independent, observations.

Today, SAMs typically employ $\sim 30 - 50$ parameters, the majority of which characterise the gas dynamics within and around halos, since that is not tracked directly in these models. With such a large number of parameters, the robustness of the physical intuition gained from such models becomes difficult to ascertain. Not only the number of parameters, but also the fact that many more equations are needed in order to capture various physical phenomena makes it enormously complex. Numerous different SAMs all match a similarly broad set of data, but often do so by invoking substantively different physical recipes and parameterizations (Somerville & Davé 2015). To mitigate this, SAMs have begun employing more sophisticated statistical approaches such as Monte Carlo Markov Chain (MCMC) parameter space searches that use Bayesian inference to obtain probability distributions and correlations. However, it is computationally infeasible to apply this approach to the entire parameter set, and thus it is typically only applied to a subset of parameters or a set of available observations (Lu et al. 2012; Henriques et al. 2013) or a “stripped-down” SAM (Benson 2014).

Hydrodynamic simulations have been gaining rapidly in popularity and importance, owing to advances in computing and input physics. Such calculations remove the need for the vast majority of SAM parameter that describe the gas dynamics, but typically still require parameters to describe “sub-grid” processes such as star formation and feedback. These days, simulations can reproduce a similarly wide range of data as SAMs (e.g. Davé et al. 2011; Vogelsberger et al. 2014; Schaye et al. 2015). While impressive, the operational complexity and computational cost of such models makes it less than straightforward to interpret the simulations in order to robustly connect physical processes with observables. Furthermore, a state-of-the-art simulation typically require millions of CPU-hours on a supercomputer, making extensive parameter space explorations prohibitive.

SAMs and simulations complement and inform each other, but the complexity of each approach present different hurdles for reaching the ultimate goal, namely a simple and intuitive understanding of the underlying physics driving galaxy evolution. As a result, the prevailing intuition in the galaxy formation community remains rooted in decades-old analytic models, even as simulations argue for significant revisions such as that star formation is fueled primarily by cold, smooth accretion (e.g. Kereš et al. 2005) and that galactic outflows drive the angular momentum distribution within disks (e.g. Brook et al. 2012), and even as observations question key aspects of the most basic paradigm such as the existence of ubiquitous large hot halos of gas around star-forming spiral galaxies (Benson et al. 2001; Crain et al. 2009). Hence despite great progress, it is becoming increasingly difficult to separate which physical processes in galaxies (and their surrounding gas) are crucial for establishing which observable properties and their evolution.

The advent of large multi-wavelength observational surveys has afforded us new opportunities to study the physical properties of galaxies in greater statistical detail. Importantly, such surveys have enabled the robust character-

isation of *scaling relations* between physical properties of galaxies such as their stars, gas, dust, metals, black holes, and dark matter. Such scaling relations are often more directly relatable to underlying physical processes than simple counting statistics. One example is the relationship between star formation rate and stellar mass (M_*), known as the “main sequence” (Noeske et al. 2007); the tightness of this relation observed out to high redshifts implies that galaxies grow mostly steadily rather than via bursts (e.g. Schreiber et al. 2015). Another example is the relationship between M_* and gas-phase metallicity (Z), which with its scatter of ~ 0.1 dex is among the tightest galaxy scaling relation known (Tremonti et al. 2004). While current SAMs and simulations broadly succeed at reproducing these relations and their evolution (Henriques et al. 2014; Schaye et al. 2015; Somerville & Davé 2015), the physical interpretation through the lens of highly complex models with many free parameters remains less than straightforward.

A recent addition to the cadre of physical models of galaxy formation is what we refer to as an “equilibrium model” (Finlator & Davé 2008; Davé et al. 2012). This is similar to a “bathtub model” (Bouché et al. 2010; Dekel & Mandelker 2014) or a “gas regulator model” (Lilly et al. 2013; Peng & Maiolino 2014), though there are non-trivial differences among these. While also analytically-based, an equilibrium model is quite different than a SAM; it does not employ a merger tree or the idea of cooling gas onto a disk via angular momentum conservation. Instead, an equilibrium model begins with a simple mass balance equation in the interstellar medium (ISM) that the inflows and outflows balance on a timescale which is very short compared to a Hubble time, with a non-trivial implication that many of the time evolution terms governing galaxy formation can be set to zero. Inflow into the ISM owes, as suggested by hydrodynamic simulations, predominantly to gravitationally-driven smooth accretion. Continual outflows eject gas from the ISM, and are incorporated as a core aspect rather than as an epicyclic add-on, as is preventive feedback owing to photoionisation or active galactic nuclei. Similarly, recycling of some outflow material back into the ISM is also a core aspect (Oppenheimer et al. 2010; Bower et al. 2012; Henriques et al. 2013). The parameters of the equilibrium model thus describe the motion of gas into and out of galaxies, which has been dubbed the *baryon cycle*.

The equilibrium model in particular makes the additional assumption that the gas reservoir in a galaxy is slowly evolving. This is motivated by hydrodynamic simulations (Finlator & Davé 2008) as well as simple theoretical expectations (Bouché et al. 2010; Dekel & Mandelker 2014), and is in accord with observations of gas content over cosmological timescales (Saintonge et al. 2013). However, this is clearly not true on shorter timescales, and for instance the gas regulator model explicitly relaxes this assumption (Lilly et al. 2013). The gas regulator model is thus more general, but its equations are significantly more complex, with a commensurate reduction in the ease of interpretation. Nonetheless it is also an instructive approach, but here for clarity we will not explicitly consider the gas reservoir, and leave it for future work.

While simple and intuitive, the baryon cycle-driven scenario forwarded by the equilibrium model and its cousins is

at face value substantively different than the merger-driven, halo-centric view of galaxies that underlies the canonical paradigm. This prevailing view has been quite successful at reproducing observations, albeit requiring dozens of free parameters to do so. A natural question then arises, can an equilibrium model also reproduce basic properties the galaxy population as observed across cosmic time? The equilibrium model has been explicitly implemented to interpret the measurements of mass-metallicity (MZ) relation (Henry et al. 2013), where they found a relative tension between the predicted MZ relation and star formation rates (SFRs) of low mass galaxies for some simple choice of baryon cycling parameters. This also motivates to ask whether the equilibrium model can directly accommodate those observations by considering these parameters as free.

In this paper, we examine how well a simple equilibrium model can match observations of key galaxy scaling relations from today until “cosmic noon” at redshift $z \sim 2$. We represent the baryon cycling parameters with free variables that we constrain against observations of the halo mass-stellar mass and mass-metallicity relations from $z = 0 - 2$, using a Bayesian MCMC approach. We show that the equilibrium model is able to match these observations within acceptable statistical bounds, using eight free parameters (minimum number we justify using the Bayesian evidence). Moreover, the same model is then able to predict the evolution of the SFR- M_* (the main sequence) from $z = 0 - 2$ in good agreement with observations, which at $z \sim 2$ has been difficult to achieve in other models. The resulting constraints on the baryon cycling parameters provide new insights into the physical processes that govern ejective and preventive feedback in galaxies over the majority of cosmic time. More broadly, our results suggest that the baryon cycling-based, mass-balance paradigm is a viable representation of the mean growth of stars and metals in galaxies over cosmological timescales, and hence the equilibrium model provides a novel and interesting framework for constructing more detailed models of galaxy evolution that may provide clearer intuition about its physics drivers.

This paper is organised as follows. In Section 2, we introduce the equilibrium model, and our chosen set of parameterisations for the baryon cycling parameters. In Section 3 and 4, we present the best fits to the observed scaling relations obtained via our MCMC, and present Bayesian evidence arguments for why these particular parameters are necessary and sufficient. In Section 5, we discuss our model predictions for higher redshifts and the general evolution of stellar and metal content of galaxies at various masses. Finally, we summarise and discuss our results more broadly in Section 6. Throughout this paper we assume a flat Λ CDM cosmology with $\Omega_m = 1 - \Omega_\Lambda = 0.27$ and $h = 0.7$ (Larson et al. 2011).

2 METHODS

2.1 The Equilibrium Model:

We present here a novel galaxy evolution model known as an equilibrium model, based on a simple set of equations that we have shown to well-approximate galaxy evolution in full hydrodynamic simulations (Finlator & Davé 2008).

The equilibrium models make the ansatz that galaxies grow along a slowly-evolving equilibrium between accretion, feedback, and star formation described by (Finlator & Davé 2008; Bouché et al. 2010; Davé et al. 2012; Lilly et al. 2013; Dekel & Mandelker 2014)

$$\dot{M}_{\text{in}} = \dot{M}_{\text{out}} + \dot{M}_*, \quad (1)$$

where the terms are the mass inflow rate into the ISM, mass outflow rate from the ISM, and star formation rate, respectively. This is essentially a mass balance equation, plus our *equilibrium assumption* that the gas reservoir in galaxies is non-evolving.

Using Equation 1, one can derive equations for the star formation rate and heavy element content of a galaxy (see Davé et al. 2012, and the Appendix):

$$\dot{M}_* = \frac{\zeta \dot{M}_{\text{grav}} + \dot{M}_{\text{recyc}}}{1 + \eta}, \quad (2)$$

$$Z_{\text{ISM}} = \frac{y \dot{M}_*}{\zeta \dot{M}_{\text{grav}}} \quad (3)$$

where \dot{M}_{grav} is the gravitational (baryonic) inflow of dark matter halos obtainable from robust dark matter-only simulations (Dekel et al. 2009), y is the metal yield derived from models of stellar nucleosynthesis (Asplund et al. 2009), and \dot{M}_{recyc} is the accretion rate of material that was previously ejected.

Here we consider metallicities in units of solar, and we assume that the yield is exactly solar metallicity; all metallicities would scale directly with variations in this assumption. Metals here are assumed to arise from core-collapse supernovae and reside in ISM gas, and hence are most closely related to observations of e.g. the gas-phase oxygen abundance. We further note that this model is most appropriately applied to *central* galaxies, as satellites are subject to environmentally-dependent processes that we will not consider here. In principle, satellites could be evolved within an equilibrium model by including environmentally-dependent quenching processes, but we leave that for future work and here focus on central galaxies only, for which we assume no explicit environmental dependence.

The equilibrium relations can be specified using three unknown variables that encapsulate some of the most poorly understood aspects in galaxy formation models:

- η , the mass loading factor, which is the mass ejection rate from the ISM in units of the galaxy’s star formation rate;
- ζ , the preventive feedback parameter, which quantifies how much of the gas entering the galaxy’s halo is prevented from reaching the ISM;
- t_{rec} , the wind recycling time, which quantifies the typical timescale for recycling previously ejected gas back into the ISM.

These ejective, preventive, and recycling parameters describe how feedback processes move baryons into and out of galaxies, and hence are referred to as *baryon cycling parameters*. We note that Davé et al. (2012) used a parameter defined by the enrichment of infalling gas to quantify wind recycling, but current models have tended to focus on t_{rec} (e.g. Henriques et al. 2013), hence we regarded it to be

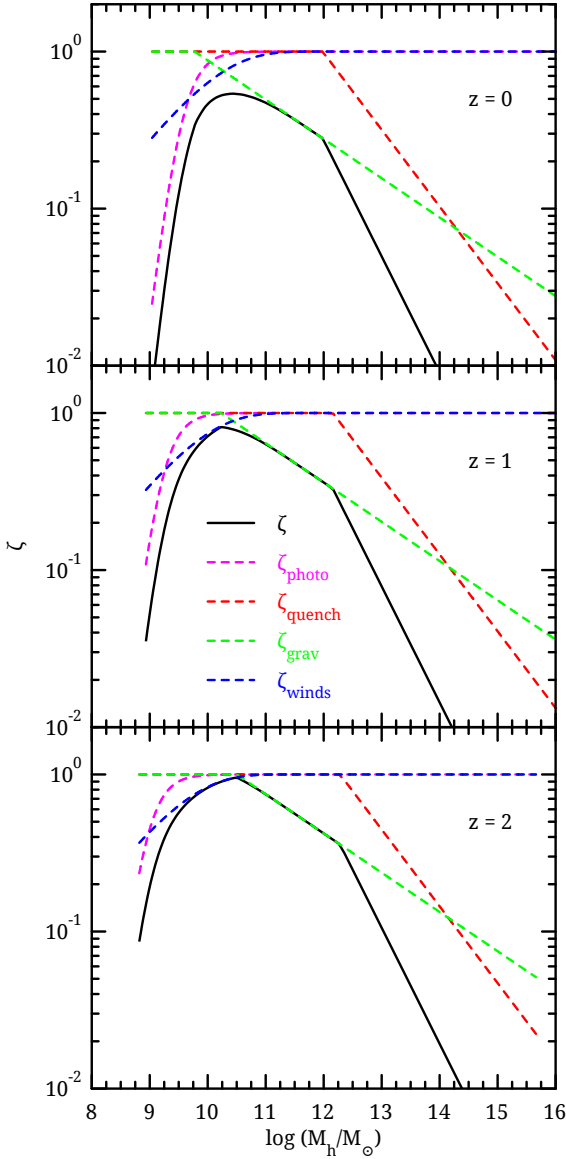


Figure 1. Preventive feedback parameter ζ at $z = 0, 1, 2$, showing the contributions from each of the terms in Equation 6. This is obtained for our best-fit model described in §2.3.

interesting for our model to constrain this parameter directly.

2.2 Parameterization

The goal of the equilibrium model is to constrain the poorly-known baryon cycling parameters using observations. With little prior information on their values and dependences, we assume they have simple dependences on mass and redshift, as follows:

$$\eta = \left(\frac{M_h}{10^{\eta_1 + \eta_2 \sqrt{z}}} \right)^{\eta_3} \quad (4)$$

$$t_{\text{rec}} = \tau_1 \times 10^9 \text{ yr} \times (1+z)^{\tau_2} \left(\frac{M_h}{10^{12}} \right)^{\tau_3} \quad (5)$$

$$\zeta = \zeta_{\text{photo}} \times \zeta_{\text{winds}} \times \zeta_{\text{grav}} \times \zeta_{\text{quench}}. \quad (6)$$

ζ_{photo} reflects prevention of infall owing to metagalactic photo-ionisation, and is parameterised based on the filtering mass from Okamoto et al. (2008) as described in Davé et al. (2012). ζ_{winds} measures the prevention of gas inflow owing to energy input into circum-galactic gas by outflows (Oppenheimer et al. 2010; Narayanan & Davé 2013), and is parameterised as in Davé et al. (2012). These two quantities only impact fairly low-mass halos, so our results here are not very sensitive to these choices. Meanwhile, ζ_{grav} suppresses inflow in high-mass halos by the gas heating due to gravitational structure formation, which is well-constrained from hydrodynamic simulations (Faucher-Giguère et al. 2011; Davé et al. 2012). Finally, ζ_{quench} describes heating from physical processes that suppress star formation in massive halos such as black hole accretion (Somerville et al. 2008; Gabor & Davé 2015). The quenching mass significantly impacts our results, and hence we will leave this as a free parameter, parameterized as

$$\zeta_{\text{quench}} = \text{MIN} \left[1, \left(\frac{M_h}{M_q} \right)^{\zeta_1} \right], \frac{M_q}{10^{12} M_\odot} = (0.96 + \zeta_2 z). \quad (7)$$

We further make an ansatz that recycling shuts off at $M_h > M_q$, which is physically motivated since quenching should prevent any re-accretion. The functional form of $\zeta(M_h)$ at $z = 0, 1, 2$ is shown in Figure 1, broken down by the contributions from the various terms, with ζ_{quench} taken for our best-fit fiducial model described in §2.3.

The parameterizations of η , ζ_{quench} , and t_{rec} are mostly chosen to have generic dependences on halo mass and redshift. One choice that is not intuitive is where we utilize \sqrt{z} in the η parameterization. This was done because using just z resulted in overly rapid evolution at $z \gg 2$ when constrained to fit data at $z \leq 2$, whereas our chosen parameterization mitigates this. Another choice is the value of $M_q = 0.96 \times 10^{12} M_\odot$ at $z = 0$, which we took from Gabor & Davé (2012) as the typical halo mass where their hot gas halo quenching kicked in; had we chose a more “canonical” value of $10^{12} M_\odot$ the results would be indistinguishably different. There are undoubtedly other variations of parameterization that could have been chosen, but we will show that these prove to be a viable descriptor.

Hence we have eight free parameters that describe baryon cycling in the equilibrium model framework. Our goal is thus to constrain these parameters, thus providing insights into the physical mechanisms that govern baryon cycling.

2.3 MCMC and Datasets

In order to constrain the baryon cycling parameters, we employ a Bayesian Monte Carlo Markov Chain (MCMC) approach to simultaneously constrain all the free parameters against key observed galaxy scaling relations. We use the publicly available CosmoMC (Lewis & Bridle 2002) code, over the entire parameter space of $\{\eta_1, \eta_2, \eta_3, \tau_1, \tau_2, \tau_3, \zeta_1, \zeta_2\}$. For constraints, the observations we employ are recent measurements of two well-known galaxy scaling relations that relate the halo mass, stellar mass, and metallicity of galaxies at $z = 0, 1, 2$:

- The $M_* - M_h$ (SMHM) relation, for which we average two recent determinations from abundance matching (Behroozi et al. 2013; Moster et al. 2013), combining their uncertainties in quadrature. We note that, given a halo mass function from Λ CDM and the assumption of abundance matching, this is equivalent to constraining to the stellar mass function.

- $M_* - Z$ relation (MZR), for which we use $z = 0$ data as determined from direct abundance measures in stacked SDSS spectra (Andrews & Martini 2013), and for $z = 1$, we use the data from Zahid et al. (2014) with 0.1 dex uncertainties and rescaling the saturation metallicity to be the same as that in Andrews & Martini (2013) (≈ 8.69 , which is comparable to the solar metallicity value). The rescaling is justified owing to the large variations in absolute calibrations among different metallicity indicators (Kewley & Ellison 2008). At $z \approx 2$, we employ measurements from both Keck Baryonic Structure Survey (KBSS) (Steidel et al. 2014) and MOSFIRE Deep Evolution Field (MOSDEF) survey (Sanders et al. 2015), but these data sets' calibrations are even less certain because the physical conditions in the ISM at those epochs may be substantially different than in today's galaxies where those indicators are calibrated. To account for this, we take the average of the observed binned mass-metallicity data sets for their two quoted calibrations (N2 and N2O2), with errors enclosing the total uncertainties among both calibrations.

- The $M_* - \text{SFR}$ relation, often called the star-forming galaxy main sequence (MS; Noeske et al. 2007). We compare to observations from Speagle et al. (2014) at $z = 0$, and a combination of Whitaker et al. (2014) (blue points) and Schreiber et al. (2015) (green points) data sets, adding an additional 0.14 dex in systematic uncertainties computed by the variance between the two data sets, at $z = 1, 2$. All these data sets are for *star-forming* galaxies only, hence we do not use any data points beyond the quenching mass M_q at that redshift, i.e. we restrict the fit to the range $10^9 M_\odot \lesssim M_* \lesssim M_q$. However, for comparison we still show the data and model beyond M_q . For further comparison, we also show the measurements of stellar mass-SFR relation by Salim et al. (2007) for $z = 0$ and Speagle et al. (2014) for $z = 1, 2$.

We constrain our model parameters by maximizing the likelihood function $L \propto \exp(-\mathcal{L})$, where \mathcal{L} is estimated from

$$\mathcal{L} = \frac{\chi^2}{2} = \frac{1}{2} \sum_{\alpha=1}^{n_{\text{obs}}} \left[\frac{\Gamma_\alpha^{\text{obs}} - \Gamma_\alpha^{\text{th}}}{\sigma_\alpha} \right]^2 \quad (8)$$

where Γ_α represents the set of n_{obs} data used in this work and σ_α are the corresponding error-bars. We then run a number of separate MCMC chains to maximize L until the usual Gelman and Rubin convergence criterion (An et al. 1998) is fulfilled.

3 MCMC CONSTRAINTS: BEST-FIT VALUES

Using CosmoMC, we obtain statistically robust constraints on the baryon cycling parameters, as listed in Table 1. The best-fit model is shown in Figure 2, compared to our set of constraining data at $z = 0, 1, 2$ in the two left panels. The use of MCMC mitigates the issue of solutions being caught in local minima. The overall agreement is quite good,

Parameters	Best-fit value and 2- σ errors
η_1	$10.98_{-0.20}^{+0.11}$
η_2	$0.62_{-0.11}^{+0.13}$
η_3	$-1.16_{-0.13}^{+0.15}$
τ_1	$0.52_{-0.11}^{+0.50}$
τ_2	$-0.32_{-0.41}^{+0.13}$
τ_3	$-0.45_{-0.14}^{+0.25}$
ζ_1	$-0.49_{-0.19}^{+0.18}$
ζ_2	$0.48_{-0.26}^{+0.28}$

Table 1. MCMC results: best-fit values and 95% confidence limits on the all eight parameters.

with a reduced chi-squared value of $\chi_\nu^2 \approx 1.64$. We use the Bayesian evidence to demonstrate that removing any one of these parameters is not statistically favored (see §4.1).

In detail, there are small systematic discrepancies among the various data. In the $M_* - M_h$ relation, our model does not reproduce the highly peaked behavior seen at $M_h \sim 10^{12} M_\odot$ (also reported by Henriques et al. 2013; Schaye et al. 2015), which corresponds to the sharpness of the cutoff in the stellar mass function above L^* . This peakiness is driven by the Behroozi et al. (2013) determination, whereas the Moster et al. (2013) determination is in better agreement with our predictions. We have also checked that, when constraining the model against $z = 0$ data alone, it can reproduce the observed peak in SMHM quite accurately. But when we try to match the galaxy properties for all epochs up to $z = 2$, the best-fit MCMC results underpredicts this peak at $z = 0$. Given the increasing uncertainties at high redshifts, this might be avoided by putting some extra weight on the $z = 0$ constraints in the MCMC run. Again the equilibrium model does not account for galaxy mergers, while they can contribute (perhaps little) to the total stellar mass of a galaxy. Then the added stellar content can help to match the observed peak better. In our future work we will try to incorporate such effects. Overall, the $M_* - M_h$ relation shows a faint-end slope and bright-end cutoff that well matches data, at all redshifts shown.

The mass-metallicity relation also shows good agreement, at least at $z = 0, 1$. At $z = 2$, it appears the observations are slightly below the inferred value, but given the calibration uncertainties we do not take this discrepancy too seriously. A key trend that is predicted by our model is that the turnover M_* increases with redshift while the faint-end slope remains similar, which is in agreement with that inferred from observations by Zahid et al. (2014). More broadly, the simultaneous agreement of the faint-end slope of the $M_* - M_h$ relation and the mass-metallicity relation is non-trivial. Simulations that match the mass-metallicity faint end tend to have too shallow a faint end for $M_* - M_h$ (or equivalently, too steep a faint end for the stellar mass

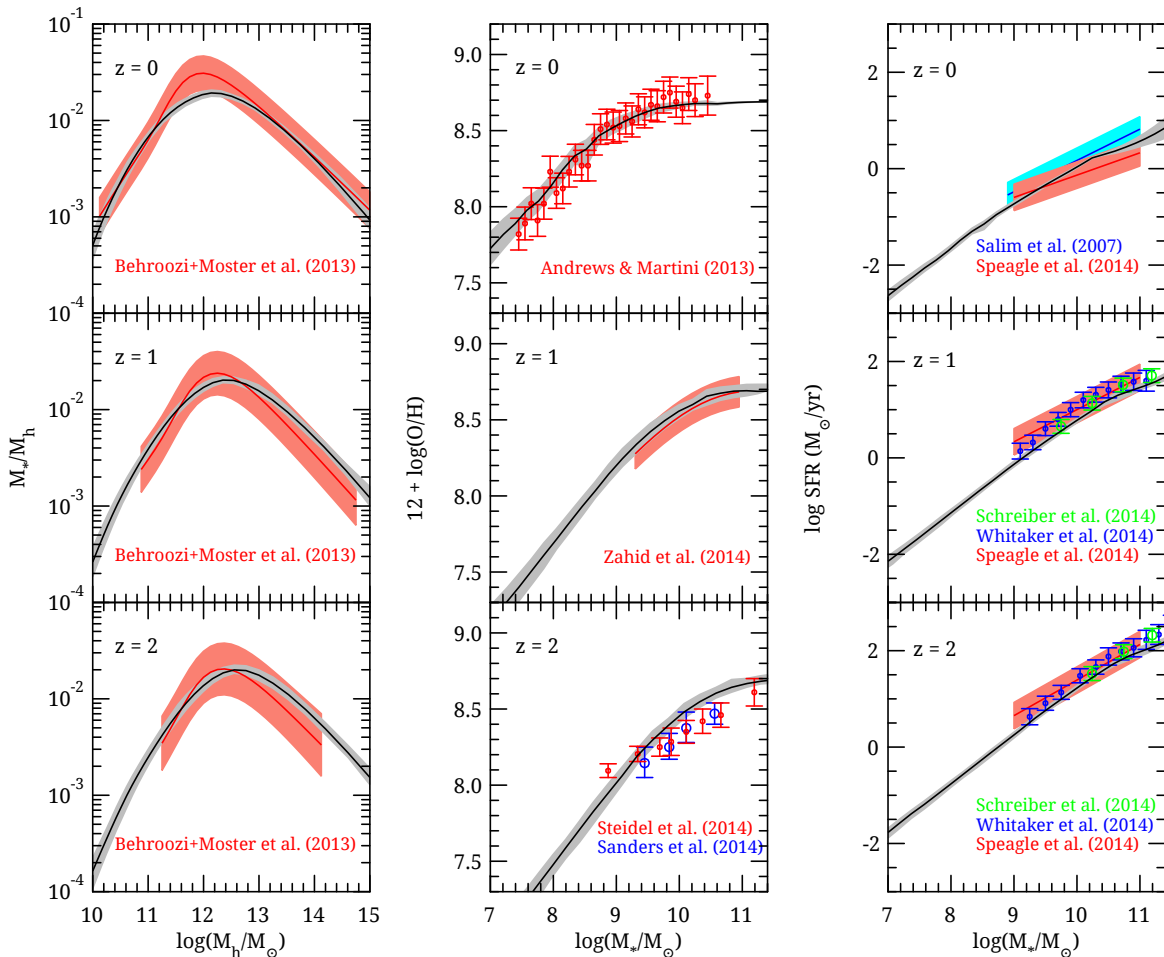


Figure 2. The marginalized posteriori distribution predicted from MCMC constraints on our equilibrium model for galaxy scaling relations at $z = 0, 1, 2$. Left panel: The stellar mass–halo mass (SMHM) relation; middle panel: mass–metallicity relation (MZR); and right panel: the SFR– M_* relation (MS). The solid black lines denote the best-fit model and the gray shaded regions correspond to their $2\text{-}\sigma$ confidence limits for all panels. The observational determinations utilized as MCMC constraints are shown as the red line with 1σ uncertainties (in the case of published fitting relations) or data points with 1σ errors (in the case of direct determinations). The specific observations employed are described in §2.3.

function; Davé et al. 2011). Increasing outflows in low-mass galaxies to better match $M_* - M_h$ results in too steep a mass–metallicity relation (Davé et al. 2013). Avenues to mitigate this include some additional preventive feedback not currently arising in simulations (Torrey et al. 2014), or a lower efficiency of converting gas into stars at low masses (Brooks et al. 2007; Gnedin & Kravtsov 2010).

The predicted MS evolves upwards in SFR at a given M_* with a mostly invariant slope, in general agreement with observations. The amplitude evolution is broadly consistent with observations, though it tends to be somewhat low compared to observations at high- z (as also seen in Henry et al. 2013), by no more than a factor of 2. We will show in §4.3 that a better match can be achieved to the MS, at the expense of a poorer match to the MZR, which may still be acceptable given the more substantial systematic uncertainties on metallicity measures in higher- z galaxies. The amplitude evolution of the MS out to $z \sim 2$ has proved particularly difficult for both semi-analytic models and simulations to match, generally showing discrepancies at the factor of 2–4 level at $z \sim 2$ when constrained (or predicted) to

match at $z \sim 0$ (Davé 2008; Sparre et al. 2015). Hence the level of agreement achieved by the equilibrium model from $z \sim 0 - 2$ is comparable to or better than in SAMs or simulations, which is a noteworthy success given its simplicity. We explore MS evolution to higher redshifts in §5.2.

4 ASSESSING THE MCMC FIT

4.1 Are all the parameters necessary?

As described in §2.3, we have chosen to represent our baryon cycling parameters with eight free parameters. The resulting reduced $\chi^2 \sim 1.6$ shows that these parameters are sufficient to achieve a good statistical match. A natural question then to ask is whether all of these eight parameters are formally necessary. We use the Bayesian evidence to assess this.

For a given model M with the data \mathbf{D} and a set of parameters Θ , one can estimate the posterior probability density of the model parameters from the Bayes’ theorem

Model	$\ln \mathcal{Z}$	\mathcal{K}	χ^2/DOF
<i>True</i>	-15.54 ± 0.15		1.64
<i>Null</i> ($\eta_1 = 12$)	-29.42 ± 0.16	$> 10^6$	6.82
<i>Null</i> ($\eta_2 = 0$)	-22.31 ± 0.15	$> 10^2$	5.23
<i>Null</i> ($\eta_3 = -1$)	-17.06 ± 0.13	5	2.09
<i>Null</i> ($\tau_1 = t_H$)	-18.63 ± 0.14	22	3.11
<i>Null</i> ($\tau_2 = 0$)	-17.97 ± 0.13	11	2.59
<i>Null</i> ($\tau_3 = 0$)	-18.93 ± 0.15	30	3.48
<i>Null</i> ($\zeta_1 = 0$)	-27.31 ± 0.14	$> 10^5$	6.17
<i>Null</i> ($\zeta_2 = 0$)	-19.84 ± 0.15	74	4.03

Table 2. MultiNest results: the mean and standard deviation of the Bayesian evidence and corresponding χ^2 values for the *true* model with eight parameters and the *null* hypotheses with seven parameters. The Bayes factor \mathcal{K} is the ratio of the evidences between the *true model* and the *null model*. It is > 1 in all cases, formally indicating the preference for the our eight-parameter model, although the inclusion of η_3 and τ_2 is only weakly preferred. Note that, the baryon cycling parameters for *true model* are constrained to have best-fit values of $\eta = \left(M_h/10^{10.98+0.62\sqrt{z}}\right)^{-1.16}$; $t_{\text{rec}} = 0.52 \times 10^9 \text{yr} \times (1+z)^{-0.32} (M_h/10^{12})^{-0.45}$; and $\zeta_{\text{quench}} = [M_h/(0.96 \times 10^{12} + 0.48z \times 10^{12})]^{-0.49}$

as (Feroz & Hobson 2008; Feroz et al. 2013)

$$\Pr(\Theta|\mathbf{D}, M) = \frac{\Pr(\mathbf{D}|\Theta, M)\Pr(\Theta|M)}{\Pr(\mathbf{D}|M)} \quad (9)$$

where, $\Pr(\mathbf{D}|\Theta, M) \equiv L(\Theta)$ is the likelihood of the data, $\Pr(\Theta|M) \equiv \pi(\Theta)$ is the prior, and $\Pr(\mathbf{D}|M) \equiv \mathcal{Z}$ is the Bayesian evidence. The evidence is then determined by calculating the average of the likelihood over the prior for that model (Feroz & Hobson 2008; Feroz et al. 2009):

$$\mathcal{Z} = \int L(\Theta)\pi(\Theta)d^D\Theta \quad (10)$$

where, D is the dimension of the parameter space. The evidence penalized models with more parameters via an increased volume of the likelihood posterior, while it penalizes models that fit poorly by a lowered likelihood. Assuming there is no strong a priori reason for favoring one model over another, the selection between two models can thus be assessed by comparing their evidences (Weinberg 2009; Feroz et al. 2013). If the evidence \mathcal{Z}_1 for model M_1 is larger than the evidence \mathcal{Z}_2 of the model M_2 , we can say the former model is statistically more favored than the later. This can be quantified by the Bayes factor $\mathcal{K} = \mathcal{Z}_1/\mathcal{Z}_2$; $\mathcal{K} > 1$ means that M_1 is more preferable by the data under consideration than M_2 .

We define a *null model* by fixing any single one of the eight parameters as follows: $\{\eta_1 = 12, \eta_2 = 0, \eta_3 = -1, \tau_1 = t_H, \tau_2 = 0, \tau_3 = 0, \zeta_1 = 0, \zeta_2 = 0\}$, where t_H is the Hubble time i.e. the age of the Universe at a given redshift.

We then vary all other seven parameters to obtain a best fit, and calculate the Bayesian evidence using the MultiNest (Feroz & Hobson 2008; Feroz et al. 2009) code. We then compare this to the evidence using all eight parameters to decide whether this given parameter is necessary, or whether it can simply be set to a “natural” value. In most cases, we take the natural value to be the one that removes the dependence on the quantity (e.g. redshift or halo mass), though in several cases we choose a value that is canonically preferred.

In Table 2, we compare the evidences between our current model with eight parameters (*true model*) and the eight *null models*. Here, the Bayes factor \mathcal{K} is the ratio of the evidences between the *true model* and the *null model*. We also show the corresponding χ^2 -values over the degrees of freedom (DOF). The “true” (eight-parameter) model has a reduced $\chi^2 = 1.64$, while the null models have a higher value. But it is still necessary to calculate the evidence to determine if the lower χ^2 in the true model is outweighed by increased freedom of having more parameters.

Table 2 shows that the evidence is always larger for the *true* model than any of the *null* hypotheses. This suggests that all eight parameters are formally necessary in order to better constrain the galaxy formation model. Given the acceptable value of the reduced $\chi^2 \approx 1.6$, this further suggests that these eight parameters are sufficient to describe the fitted observations. The Bayes factor \mathcal{K} is very large for some cases like the quenching feedback parameters (ζ_1, ζ_2) or the normalization of the mass loading factor (η_1, η_2), suggesting that the inclusion of those parameters is strongly favored for obtaining a good fit. On the other hand, one can see that the inclusion of other parameters e.g. the recycling parameters is only weakly preferred. It is also somehow evident from the fact that, the majority of our observational constraints are at high masses above where the quenching effect is significant, whereas our model shuts off the recycling at that mass scale.

4.2 Are all the parameters independent?

The Bayesian MCMC approach has the advantage of being able to view the posterior probability for each parameter, and particularly to determine whether parameters are significantly correlated. This offers another way to ensure the parameterizations we have adopted are necessary and sufficient.

Figure 3 shows the 1-D (diagonal panels) and 2-D (off-diagonal panels) marginalized posterior probability distributions for all eight parameters. The generally circular appearance of the best-fit covariances indicates that none of parameters are significantly correlated with each other. The concentrated peak in each panel shows that, while other solutions exist, the best-fit solution is strongly preferred. These panels also shows the range considered for each variable, over which we have assumed a flat prior; the best-fit values are comfortably within the assumed range. This demonstrates that the parameterizations as well as the range for the prior that we have taken are reasonable choices.

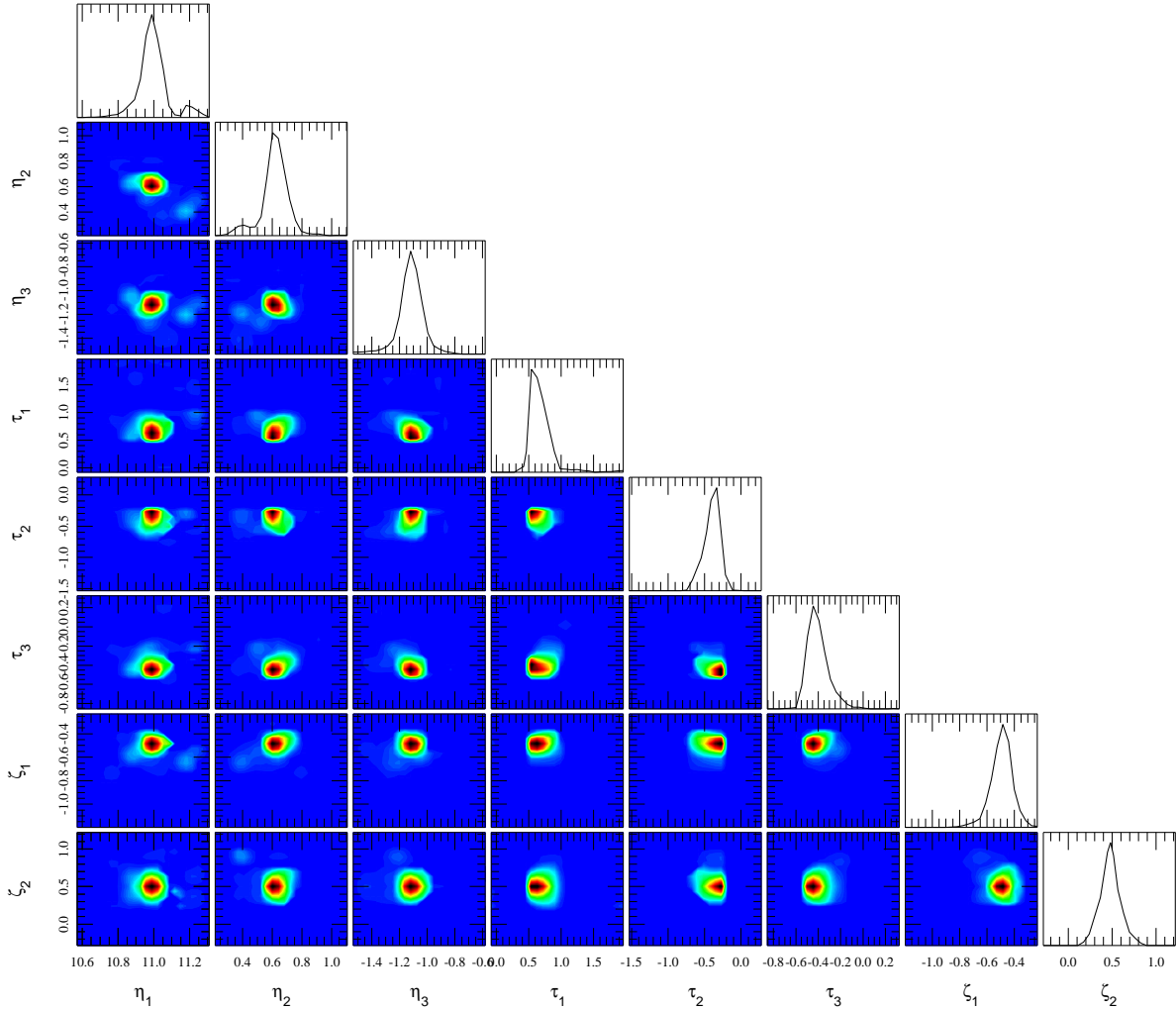


Figure 3. Marginalized 2-D contours for all eight parameters from MCMC analysis. Panels along the diagonal show the 1-D marginalized probability distributions for each parameter, while the off-diagonal panels indicate the joint probability distributions of them.

4.3 Are all the data required?

Here we examine whether all 3 scaling relations we have considered are necessary to obtain a good fit. The way we assess this is to fit only two of the three relations, and determine how well the resulting best-fit model *predicts* the third.

Figure 4 shows the result of fitting only to the SMHM and MZR relations, and predicting the MS. The solid line is the new best-fit, while the dashed line shows the original model fit to all three data sets reproduced from Figure 2 for comparison. The overall fit remains mostly unchanged. The agreement is slightly worse for the MS, as might be expected since we no longer utilizing that data as a constraint. However, the fit is marginally better for other data sets. In the end, χ^2_ν for this model fit is 1.51 just considering the fit to the SMHM and MZR. The overall χ^2_ν for all three data sets is 1.68, which is slightly worse, but still within acceptable uncertainties. This demonstrates the rather remarkable result that even just fitting to two of these scaling relations (SMHM and MZR), the equilibrium model is able to *predict* the independently-determined MS to good accuracy.

Now, one could argue that constraining to the stellar mass growth as a function of halo mass out to $z = 2$ nat-

urally assures that the SFR will be reproduced, assuming that halo mass growth is properly tracked. Also note that, for our model, matching the MZR for a given M_* essentially forces to match the SFR via Equation 3. While true in principle, current models that broadly match the SMHM relation and its evolution still fail to match the MS evolution at the $\gtrsim \times 2$ level (Weinmann et al. 2012). Hence the agreement predicted by the equilibrium model to better than a factor of 2 from $z = 0 - 2$ is non-trivial.

To more fully explore our model, we can fit to the SMHM relation and the MS, and then predict the MZR. In this case, the metallicity is not being used as a constraint anywhere, so we can assess whether the metallicity evolution is predicted correctly in this model. Figure 5 shows the result. The fit to the MZR is still excellent at $z = 0$, and is not much different at $z = 2$, but tends to overshoot the $z = 1$ data somewhat by having too low a turnover mass. Hence it is not quite as good as before, but given the systematic uncertainties in metallicity measures (Kewley & Ellison 2008) it is likely still acceptable. The general trend of an MZR with an upwardly-evolving MZR turnover mass remain the same, which shows that this is a generic prediction for an

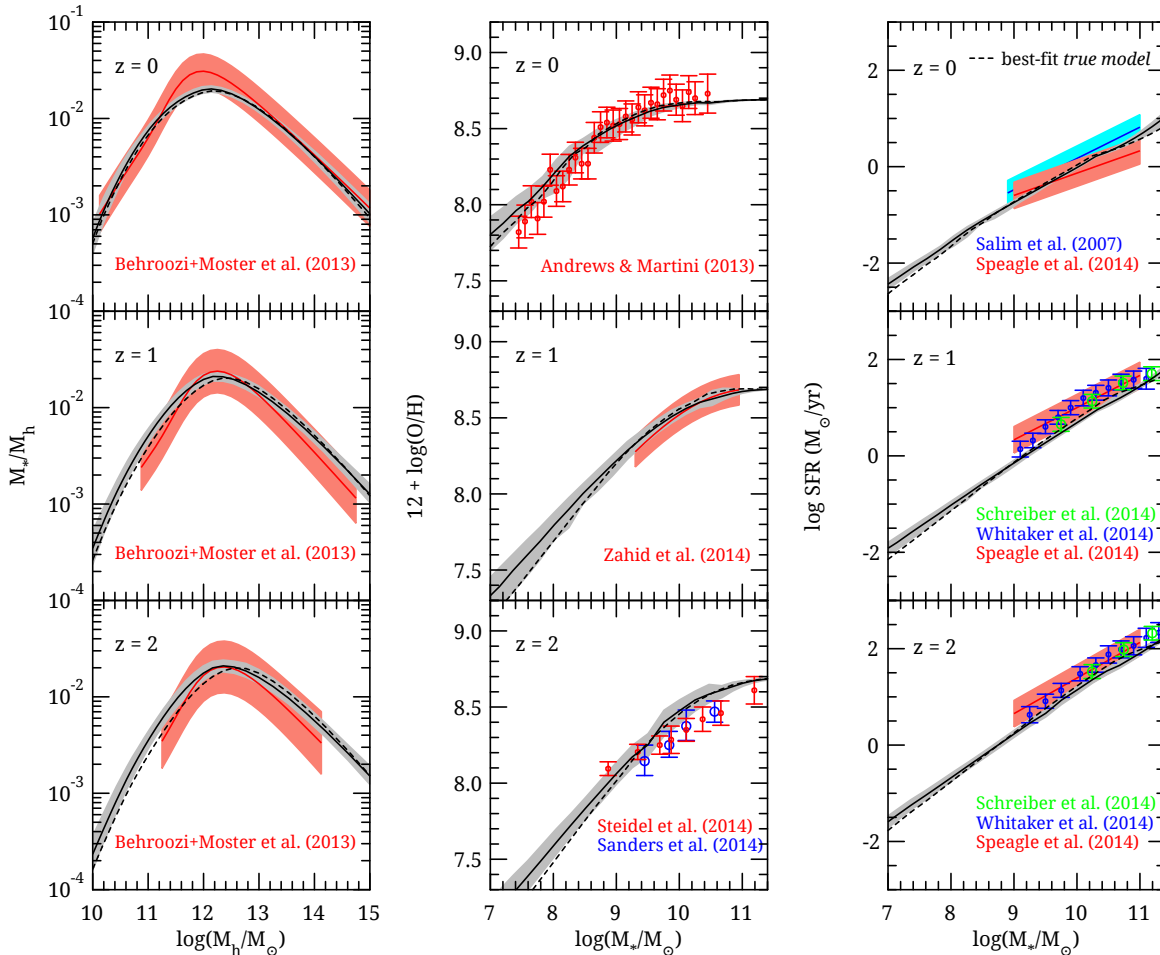


Figure 4. The marginalized posteriori distribution from MCMC analysis for our considered scaling relations at $z = 0, 1, 2$, here fitting only to two relations, namely SMHM and the MZR. Data are shown as described in Figure 2. The best-fit *true* model with all three data sets from Figure 2 is also plotted here as short-dashed lines for comparison.

equilibrium model with reasonable constraints. So we find that, this model can match the SFR data more accurately at least for low-mass galaxies, but overpredicts the MZR owing to Equation 3 (a similar trend is also seen in Henry et al. 2013). This could happen due to the yield value assumed here and can be avoided by taking a smaller y or making it as a free parameter (effectively equivalent to varying the IMF; Narayanan & Davé 2013) which will be incorporated in the future work. We further note in this case a steeper turn-down in the SMHM relation at low masses at $z = 1, 2$, which agrees better with the observationally-constrained determinations of this. The resulting χ^2_ν just fitting to SMHM and MS is 1.48, while χ^2_ν over all data sets (including the MZR) is now 2.01. Hence the fit has degraded slightly overall, but remains acceptable.

Figure 6 lastly examines the results for the final permutation, namely constraining to the MZR and MS and predicting the SMHM relation. In this case we obtain a very good fit to the constrained relations ($\chi^2_\nu = 1.55$), now predicting the MS amplitude at $z = 2$ extremely well. However, the predicted SMHM relation, while similar at $z = 0$, increasingly overshoots the observationally-determined values to higher redshifts, particularly at high masses. For this case, the overall $\chi^2_\nu = 1.84$ when considering all three data sets.

These permutations demonstrate that the equilibrium model can fit any two of the three scaling relations very well, and the third relation is then also fairly well predicted. Interestingly, the $z = 0$ values are the most closely predicted ones. Note that we have not constrained our model to match better at $z = 0$ than at any other redshift; all the data at all the redshifts are weighted equivalently (i.e. by their respective uncertainties) in our MCMC fit. Meanwhile, fits are degraded relative to the data in our model mostly when considering higher redshifts, where of course systematic effects in observational determinations of these galaxy properties likely are larger. It will be interesting to see, as data at higher redshift improves, whether observational determinations at higher redshifts become more self-consistent between these three scaling relations within the context of the equilibrium model, as they are at $z = 0$.

Overall, the fact that the equilibrium model constrained to fit two of the scaling relations can reasonably well predict the third supports the idea that its underlying framework is a viable representation for how the mean galaxy population evolves. While one would prefer a fit of $\chi^2_\nu < 1$ to claim formally perfect agreement, the values we obtain by fitting all three or any two of the three data sets is still remarkably good ($\chi^2_\nu \lesssim 2$) when considering the numerous difficult-to-

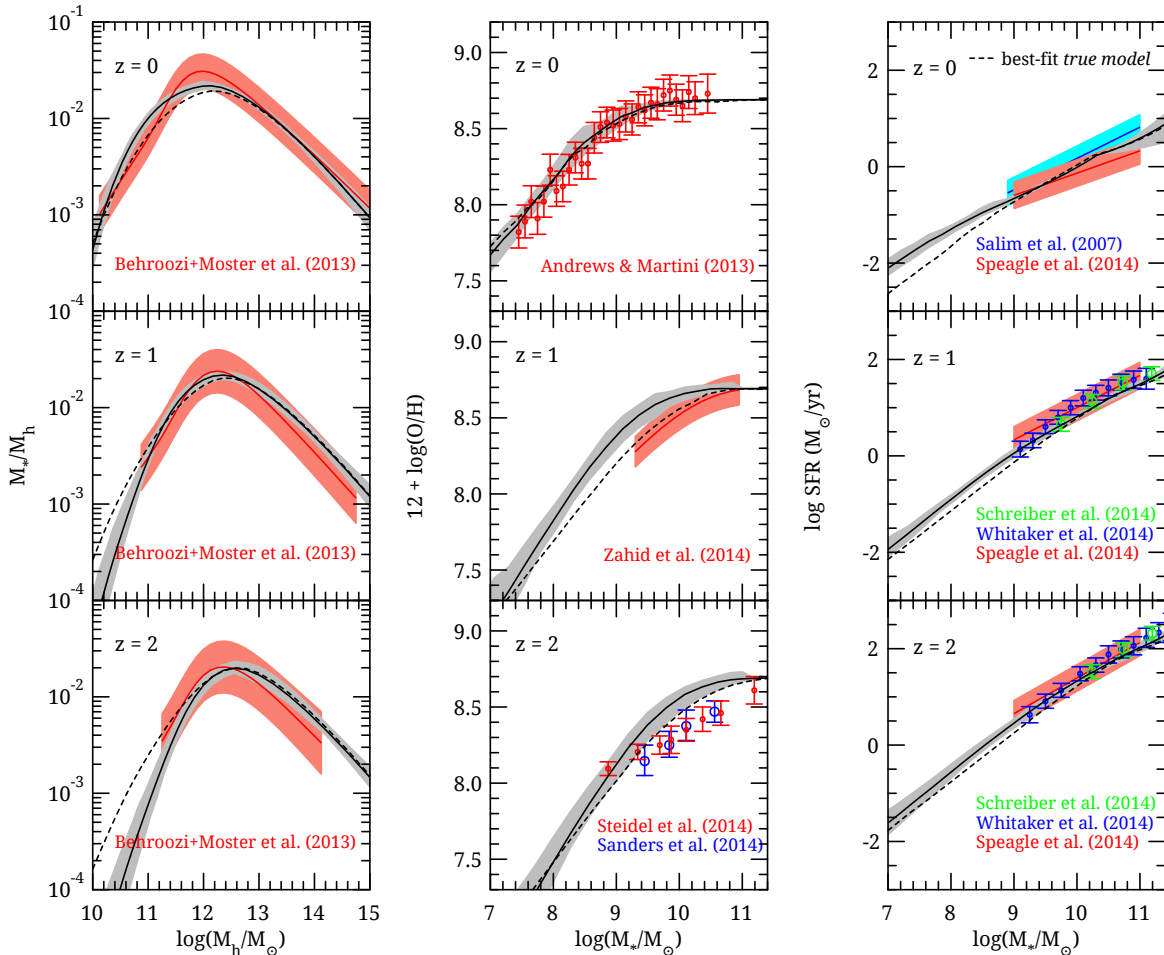


Figure 5. The marginalized posteriori distribution from MCMC analysis for our considered scaling relations at $z = 0, 1, 2$, here fitting only to SMHM and the MS. Data are shown as described in Figure 2.

quantify systematic effects present in the data particularly to higher redshifts.

5 IMPLICATIONS AND DISCUSSION

5.1 Implications for baryon cycling parameters

The crucial power of the equilibrium model is its ability to constrain the baryon cycling parameters directly from data in a statistically robust manner. This then provides insights into the physics of feedback processes, and constraints for more detailed models of inflows and outflows. Here we examine the predicted halo mass and redshift dependences of the baryon cycling parameters, and briefly discuss some physical implications. This is intended to provide a brief illustration of how an equilibrium model can be useful to obtain insights into galaxy formation processes, but of course there are many more such aspects that we will leave for future work.

Figure 7 shows the dependence of the baryon cycling parameters on stellar and halo mass in the left panel and right panel, respectively, at $z = 0, 1, 2$. While the parameters are directly constrained based on the halo mass, we have

convolved these with our predicted $M_* - M_h$ relation to obtain the stellar mass dependences.

The ejective feedback parameter scales as $\eta \propto M_*^{-0.5}$ at low masses, which is intermediate between scalings expected for momentum- and energy-driven winds, suggesting that both effects are in play (Murray et al. 2010). This is broadly similar to scalings assumed or generated in cosmological simulations that match a wide variety of data, which have for instance assumed $\eta \propto M_*^{-1/3}$ (Davé et al. 2011) to $\eta \propto v_c^{-2} \propto M_*^{-2/3}$ (roughly; Vogelsberger et al. 2014). It is also in agreement with scalings predicted in ab initio simulations of stellar-driven outflows from the Feedback in Realistic Environments suite (Faucher-Giguère et al. 2013; Hopkins et al. 2014), suggesting that the interplay of radiation pressure and supernovae energy that drive winds in those single-galaxy simulations is plausible. This illustrates how the equilibrium model thus provides a way to directly connect and constrain the predictions from high-resolution individual galaxy simulations with galaxy population statistics across cosmic time. Also we find that, the model robustly prefers η_2 to be positive, which implies that galaxies are less effective at driving outflows at high redshifts than at lower redshifts. Such a dependence could reflect the tendency for outflows to be less efficient in galaxies with

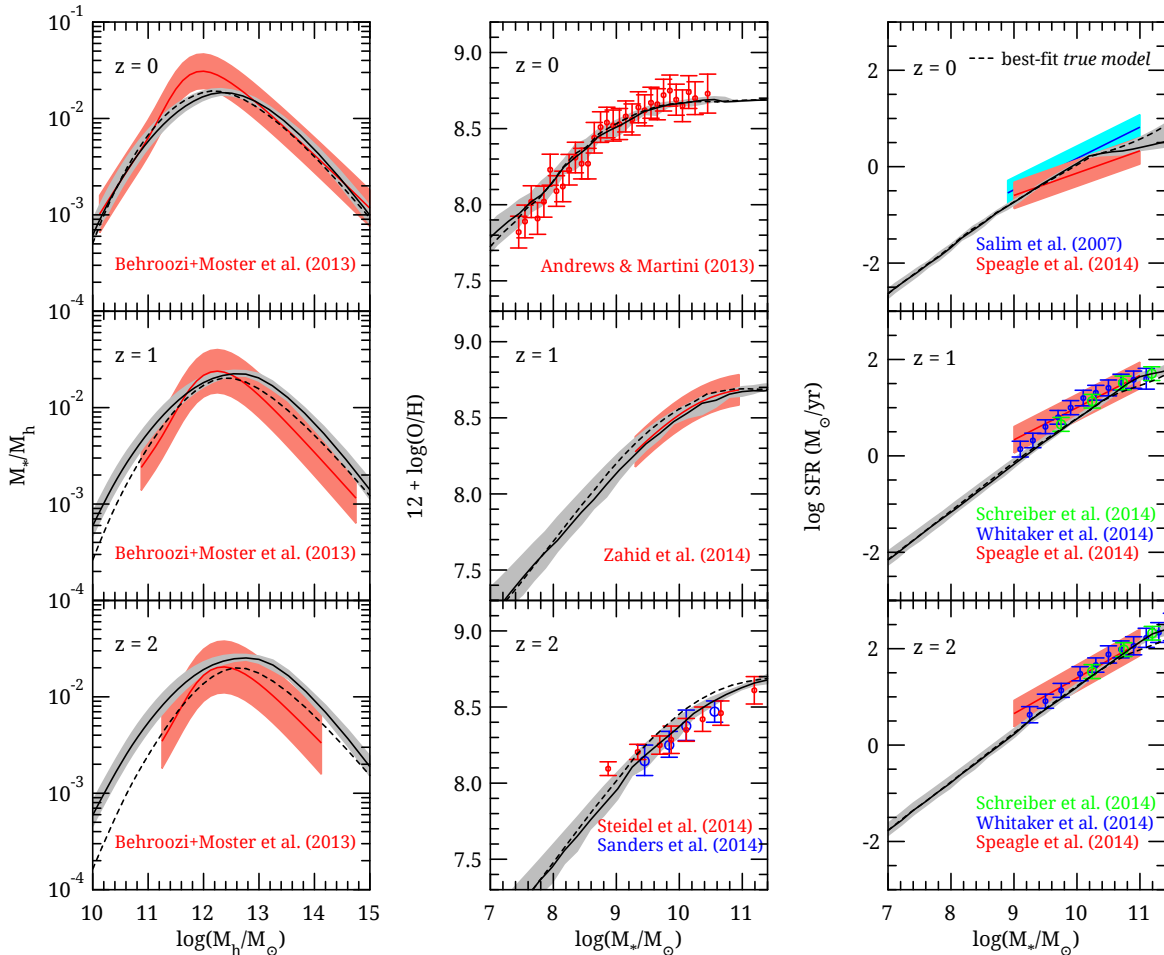


Figure 6. The marginalized posteriori distribution from MCMC analysis for our considered scaling relations at $z = 0, 1, 2$, here fitting only to the MZR and the MS. Data are shown as described in Figure 2.

higher gas fractions (Creasey et al. 2015) or lower metallicities (Schaye et al. 2015).

The recycling time distribution is currently much debated. Our model predicts that it is nearly invariant with redshift, and scales as $t_{\text{rec}} \propto M_h^{-0.5}$. This is a significantly weaker dependence than predicted in cosmological hydrodynamic simulations (Oppenheimer & Davé 2008) and inferred in SAMs (Henriques et al. 2013) of $t_{\text{rec}} \propto M_h^{-1}$, or even that predicted from simple gravitational binding arguments. Zoom simulations that employ supernova heating to drive outflows from Christensen et al. (2015, in preparation), in contrast, predict a similarly weak dependence of t_{rec} , and are likewise able to simultaneously match the $M_* - M_h$ relation (Munshi et al. 2013) and the MZR (Brooks et al. 2007). The interplay between outflows and ambient circumgalactic gas remains a difficult numerical problem for current hydrodynamical codes and depends strongly on the particular implementation of wind driving and hydrodynamic technique. Hence the equilibrium model can provide important constraints on such difficult-to-model processes.

The quenching mass is another key parameter in galaxy formation models. Dekel et al. (2009) argued for a quenching mass around $10^{12} M_\odot$ out to $z \sim 1 - 2$, before which it increases with redshift owing to cold streams penetrating hot halos. Simulations by Gabor & Davé (2012) as-

sumed quenching happens once a hot gaseous halo forms, and also find a quenching mass around $10^{12} M_\odot$ that increases mildly with redshift. SAMs have long implemented a halo mass above which putative AGN feedback is able to heat gas, which again is typically $\sim 10^{12} M_\odot$ and mostly invariant with redshift (Croton et al. 2006; Bower et al. 2006; Somerville et al. 2008). Our model predictions are generally in agreement, with a slowly-increasing quenching mass with redshift. Notably, however, our results are inconsistent with a single invariant quenching mass at all redshifts (§4.1). This indicates that quenching is not purely a function of halo mass, but depends on some other property that scales slowly with quenching mass over time.

To further investigate why the equilibrium model robustly prefers different scaling relations than those obtained from SAMs and hydro-simulations, we compare the Bayesian evidence of our current *true* model with the evidences from different *null* models. We choose the null values for the parameters associated with η and t_{rec} in a fashion that they resemble the models with momentum-driven scaling $\eta \propto M_*^{-1/3}$ (Davé et al. 2011), energy-driven scaling $\eta \propto M_*^{-2/3}$ (Vogelsberger et al. 2014) and a steeper dependence of $t_{\text{rec}} \propto M_h^{-1}$ as inferred from SAMs (Henriques et al. 2013). So instead of using the “natural” null values as previ-

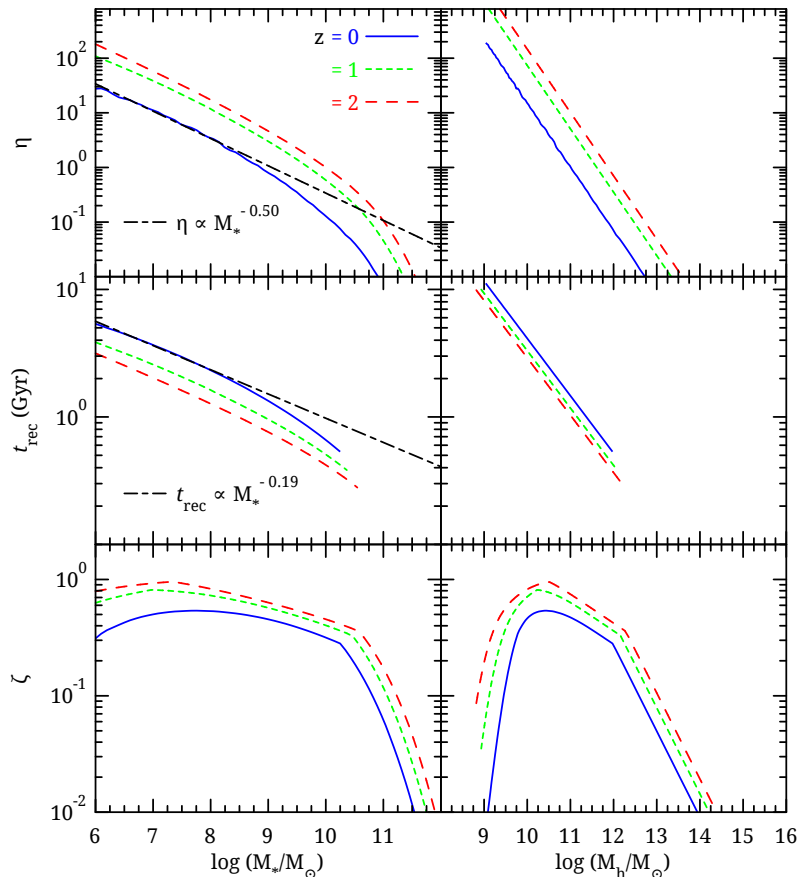


Figure 7. The dependence of the baryon cycling parameters on stellar (left panel) and halo (right panel) masses at $z = 0$ (solid blue lines), $z = 1$ (short-dashed green lines) and $z = 2$ (long-dashed red lines). For comparison, $\eta \propto M_*^{-0.50}$ and $t_{\text{rec}} \propto M_*^{-0.19}$ are also plotted by short-long-dashed lines.

ously mentioned in Table 2, we now take these models as our null ones and calculate their corresponding evidences. We have listed our results in Table 3, where one can see that pure energy or momentum-driven outflows with no redshift dependence ($\eta_2 = 0$), as assumed in those simulations, fails to give a reasonable fit to the observed data (reduced $\chi^2 \sim 8$). One can get more acceptable models with those scalings by allowing η_2 to vary (reduced $\chi^2 \sim 2$). In both cases, the energy-driven winds suppress mass and metals more at low-masses, while the momentum-driven scalings suppress less than observed. Thus an intermediate scaling ($\eta \propto M_*^{-0.5}$) is formally more favored by the data considered here. Table 3 reinforces the impression from Figure 3 that observations constrain both the mass- and redshift-dependence of galactic outflows as well as the return timescale. Judging by the Bayes factors, a redshift evolution for η is strongly favored, while our best-fit mass-dependence is more weakly (but still formally) favored over canonical alternatives. Meanwhile, our best-fits for the quenching scale and recycling are highly favored over those. Nonetheless, the Bayes factor \mathcal{K} is > 1 (also the reduced χ^2 is larger) for all null cases. This indicates that the scaling relations for baryon cycling parameters obtained from our 8-parameter model are clearly preferable to the parameterizations employed in those works.

These examples briefly illustrate how the equilibrium model can provide insights and constraints for more

physically-based models for baryon cycling processes. Alternatively, it can potentially exclude models whose baryon cycling behavior is substantially different from that predicted here, or else quantify how far off such a model would be from matching these observed galaxy scaling relations. Current simulations and SAMs have, through less rigorous parameter space exploration, arrived upon generally similar constraints as those preferred by our model, but the equilibrium model framework provides a more quantitative way to directly constrain baryon cycling from observations.

5.2 Predictions to higher redshift

So far we have seen that our model can match the observational data sets quite reasonably from $z = 0 - 2$. Due to the increasingly large observational and systematic errors, the knowledge of the galaxy population at higher redshifts is less certain, hence we have not included these observations as constraints on our model. Nonetheless, as a sanity check, we here show how our model predicts the behavior of galaxies at earlier epochs.

In Figure 8 we show our model predictions for the stellar mass–halo mass relation (left panel), mass–metallicity relation (middle panel) and SFR– M_* relation (right panel) for all the redshifts up to $z = 6$. Their redshift evolution is denoted by the solid lines with different colors for different

Model	$\ln \mathcal{Z}$	\mathcal{K}	χ^2/DOF
<i>True</i> model	-15.54 ± 0.15		1.64
<i>Null</i> model with $\eta \propto M_*^{-1/3}$ (varying η_2)	-17.30 ± 0.13	6	2.27
<i>Null</i> model with $\eta \propto M_*^{-2/3}$ (varying η_2)	-17.23 ± 0.13	5	2.18
<i>Null</i> model with $\eta \propto M_*^{-1/3}$ (keeping $\eta_2 = 0$)	-36.16 ± 0.14	$> 10^8$	8.15
<i>Null</i> model with $\eta \propto M_*^{-2/3}$ (keeping $\eta_2 = 0$)	-35.80 ± 0.14	$> 10^8$	7.92
<i>Null</i> model with $t_{\text{rec}} \propto M_h^{-1}$	-22.47 ± 0.13	$> 10^3$	5.28

Table 3. Comparison of the Bayesian evidences and corresponding χ^2 values for our *true* model with eight parameters to that obtained from different *null* models. The Bayes factor $\mathcal{K} > 1$ for all cases indicates that the *true* model is more favored over any of these null models.

redshifts as mentioned in the bottom of right panel. The $z = 0 - 2$ results are the same as the best-fit solid lines of Figure 2.

The $M_* - M_h$ relation shows a clear peak in the stellar mass–halo mass ratio which is visible at all the redshifts. The location of the peak shifts towards higher masses with increasing redshift. This is broadly consistent with the results out to $z \sim 2$ (Leauthaud et al. 2012; Behroozi et al. 2013; Moster et al. 2013), but at higher redshifts, the determinations diverge: Moster et al. (2013) suggests a continued increase in the peak stellar efficiency, while Behroozi et al. (2013) suggests a drop. Our results are more consistent with Moster et al. (2013), in part because our functional form with redshift is assumed to be monotonic. Furthermore, the amplitude of the peak efficiency decreases a bit at higher redshifts, which is in agreement with recent determinations (Behroozi et al. 2013; Moster et al. 2013; Birrer et al. 2014). For our best-fit model, the stellar mass–halo mass ratio peaks at $M_h \sim 10^{12} M_\odot$ for $z = 0$, shifting to $M_h \sim 10^{13} M_\odot$ for $z = 6$. For very high mass galaxies, we see that the stellar mass increases with increasing redshifts, since quenching feedback (ζ_{quench}) is less effective at higher redshifts. For more typical galaxies, the stellar efficiency decreases with increasing redshifts, owing primarily to stronger ejective feedback (η) at a given halo mass. This is a form of downsizing, where the peak efficiency of star formation from baryons within halos drops with time.

In the middle panel of Figure 8, we show the evolution of the mass–metallicity relation over the range $7 \leq \log(M_*/M_\odot) \leq 11.4$. Although, all the galaxies increase in both mass and metallicity as they evolve, the shape and slope of their relation is not constant with time and stellar

mass (Finlator & Davé 2008). The evolution can actually be well-described by a fixed faint-end slope, with a turnover to a flat MZR at a mass that evolves downwards with time. Such a behavior is also inferred from observations by Zahid et al. (2014), who found a turnover mass of $10^9 M_\odot$ at $z = 0$ increasing to $10^{9.7} M_\odot$ at $z \sim 1$; these values are in broad agreement with our model predictions. In our model, such a trend continues to higher redshifts, such that at $z \gg 2$ the galaxies within the observationally-accessible stellar mass range mostly lie on a power-law MZR, since the turnover mass has now exceeded $10^{11} M_\odot$. Measuring the evolution of the MZR at a fixed M_* would thus give results that are highly mass-dependent; from $z = 2 \rightarrow 0$, at $M_* = 10^9 M_\odot$ the metallicity increases by $\times 3$, where at $M_* = 10^{10.5} M_\odot$ it increases by only ~ 0.1 dex. As metallicity measures are pushed to lower masses and wider areas at high redshifts by surveys such as MOSDEF, this will present an interesting testable prediction.

The predicted evolution of the MS out to $z = 6$ is shown in the right panel of Figure 8. Our best-fit model predicts that, at a given M_* , star formation rates are increasingly higher at earlier times (Bouché et al. 2010). We also see, at late epochs, that the M_* -SFR relation shows a shallower slope at high stellar masses, which is also seen in observations (Whitaker et al. 2014). The evolution of the SFR at a given M_* slows but does not cease to the highest redshifts, in agreement with observations by Stark et al. (2013). We note that our predicted relations are for the mean SFR at any given M_* , but for large galaxies this could manifest as a small number of galaxies with high SFR while most galaxies are non-star forming; our current model does not account for such “duty cycle” effects.

Figure 9 shows the specific SFR at a fixed stellar mass of $5 \times 10^9 M_\odot$ from $z = 0 - 7$. Observational data is shown from Noeske et al. (2007); Daddi et al. (2007); Reddy et al. (2012); Stark et al. (2013); Duncan et al. (2014), with the corresponding quoted uncertainties in the figure. Our best fit-model underpredicts the sSFR slightly at $z \sim 1$, but is in good agreement at $z \sim 2$ unlike in many previous models. At higher redshifts the observations become more subject to systematic uncertainties particularly related to the contribution of nebular emission lines to the flux beyond the 4000Å break (Stark et al. 2013). Nonetheless, the general trend of a slower increase in sSFR with z at higher redshifts is in broad agreement with observations, and is in good agreement with the data from Stark et al. (2013) though slightly above observations by Duncan et al. (2014). In Figure 10, we have shown the sSFR for galaxies with different stellar masses ($M_* = 10^9, 10^{9.5}, 10^{10}$ and $10^{10.5} M_\odot$) as a function of redshift. Unlike the widely-reported difficulty for SAMs and hydro simulations (e.g. Sparre et al. 2015) to reproduce different sSFR as a function of stellar masses, the equilibrium model predicts somewhat mass-dependent sSFR at fixed redshift. This behavior is in well agreement with that obtained from several empirical models (e.g. Moster et al. 2013), at least for lower redshift range.

Overall, the predictions of the equilibrium model are in good agreement with observations from today back to the earliest observable epochs. As observations at higher redshifts improve, these will provide a more stringent test (or additional constraints) for this model. An additional caveat, as discussed in Davé et al. (2012), is that there is a period at

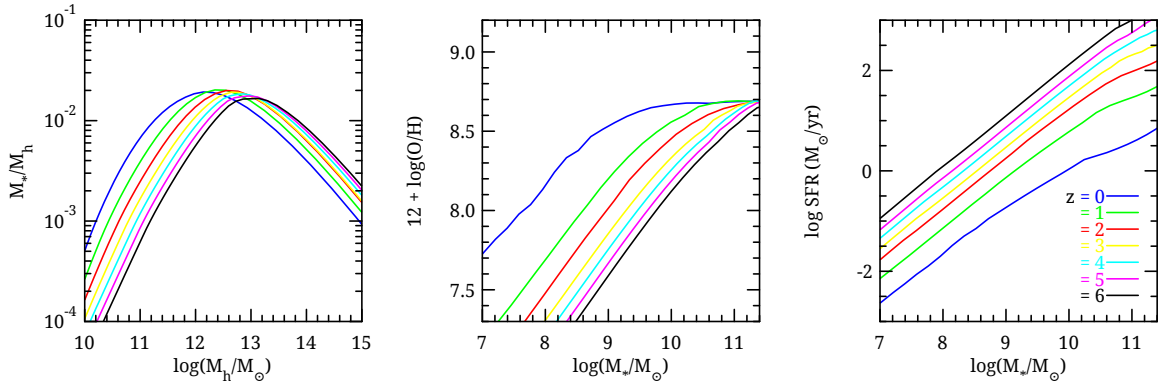


Figure 8. Model prediction for (i) $M_* - M_h$ relation (left panel), (ii) $M_* - Z$ relation (middle panel) and the M_* -SFR relation (right panel) at redshifts $z = 0$ (blue), $z = 1$ (green), $z = 2$ (red), $z = 3$ (yellow), $z = 4$ (cyan), $z = 5$ (magenta) and $z = 6$ (black). Note that, the $z = 0 - 2$ results are the same as the best-fit MCMC analysis in Figure 2, whereas the higher redshifts results are the model prediction.

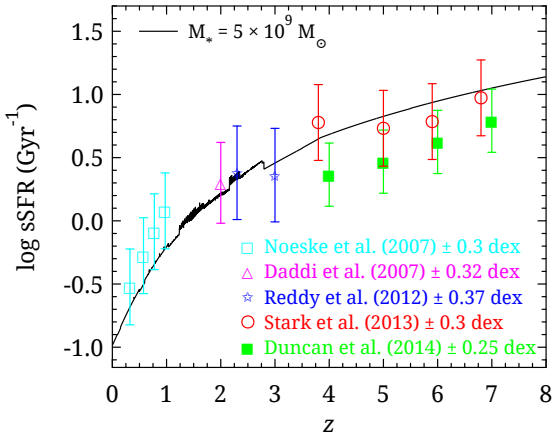


Figure 9. Specific SFR at $M_* = 5 \times 10^9 M_\odot$ as a function of redshift, compared with observations listed and described further in the text.

very early epochs where the equilibrium assumptions cannot be satisfied owing to inflow rates that exceed the galaxies’ ability to process that gas into stars and/or outflow. Observationally, this “gas accumulation epoch” is inferred to end roughly around $z \sim 4$ (Papovich et al. 2011). We expect the equilibrium model to begin to break down as observations probe the gas accumulation epoch, but so far the data are insufficient to assess this.

5.3 Evolution of stars, gas, and metals

A direct prediction of the equilibrium model is the growth of stars and metals in galaxies of various masses over cosmic time. Given that the MCMC-constrained model correctly predicts the observed evolution of key scaling relations, we can now explore the implications for this.

In Figure 11, top panel, we show the SFR evolution calculated from our best-fit model for four galaxies that have final ($z = 0$) halo masses from $10^{11} - 10^{14} M_\odot$. More massive galaxies are seen to have earlier and relatively higher peak in their evolution of SFR, consistent with the idea of

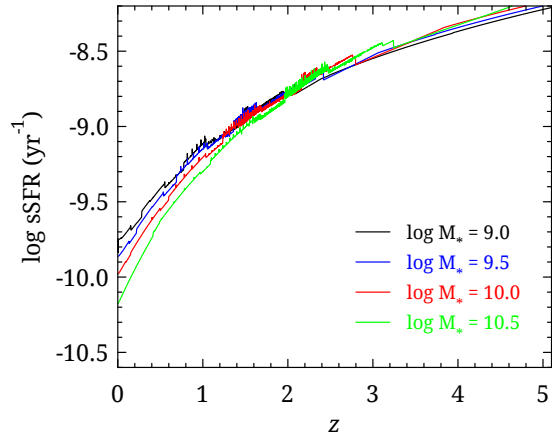


Figure 10. Specific SFR as a function of redshift for galaxies with different stellar masses of $M_* = 10^9 M_\odot$ (black), $10^{9.5} M_\odot$ (blue), $10^{10} M_\odot$ (red) and $10^{10.5} M_\odot$ (green). Our equilibrium model predicts somewhat different sSFR for different stellar masses at a fixed redshift.

downsizing (Thomas et al. 2005). A typical massive galaxy of $10^{14} M_\odot$ halo is seen here to have a peak in SFR of $\sim 150 - 200 M_\odot \text{yr}^{-1}$ at $z \sim 3 - 4$. In contrast, for a Milky Way-sized halo ($10^{12} M_\odot$, green lines), the SFR peaks at $\sim 3 - 6 M_\odot \text{yr}^{-1}$ around $z \sim 1 - 2$, while at $z = 0$ it has SFR of $\sim 2 M_\odot \text{yr}^{-1}$, total stellar mass of $\sim 2 \times 10^{10} M_\odot$ and $Z = Z_\odot$. This stellar mass is lower than observed (Licquia & Newman 2015), which reflects the fact that our model does not quite produce the peaked distribution in the $M_* - M_h$ relation right around $10^{12} M_\odot$. Also, if the Milky Way halo mass is more like $2 \times 10^{12} M_\odot$ (Boylan-Kolchin et al. 2010; McMillan 2011) as has been argued, then the stellar mass would be commensurately higher and in better agreement with observations. Dwarf galaxies have increasing star formation rates with time, but still begin forming stars at $z \gg 2$.

In the bottom panel of Figure 11, we show the evolution of the metallicity. This is very rapid at the earlier stages and then slows down (Davé et al. 2006; Finlator et al. 2011; Davé et al. 2012). Once a galaxy becomes quenched,

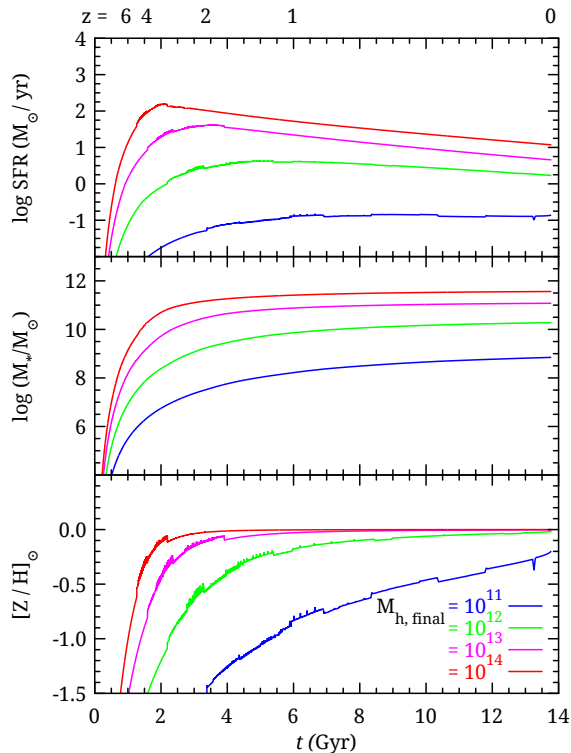


Figure 11. Evolution of stars and metals of different galaxies that have final $z = 0$ halo masses of $10^{11}M_{\odot}$ (blue), $10^{12}M_{\odot}$ (green), $10^{13}M_{\odot}$ (magenta), $10^{14}M_{\odot}$ (red). Panels from top to bottom display the evolution of star formation rate, total stellar mass and metallicities. The small fluctuations in the evolution of stars and metals indicate the effect of wind recycling implemented in this model.

its metallicity saturates, which in our model is constrained to happen at around the yield value that we assume is at solar metallicity. Recall that this predicted metallicity corresponds to the gas-phase oxygen abundance, which does not account for additional enrichment of e.g. iron from Type Ia supernovae.

Note that there are small fluctuations in the evolution of stars and metals, owing to the effect of wind recycling which takes some of the ejected material at an early time and puts it back into the galaxy after a time t_{rec} . We can also see that massive galaxies have comparatively shorter recycling times, which is qualitatively consistent with the simulation predictions (Oppenheimer & Davé 2008).

There are many potential uses for these types of equilibrium model evolutionary predictions. For instance, a common technique to obtain galaxy physical properties from broad-band data is via spectral energy distribution (SED) fitting, which critically relies on an assumed input star formation history (SFH). A single galaxy’s equilibrium model run takes just seconds, so can quickly provide realistic SFHs constrained on-the-fly while performing SED fits. This provides greater realism compared to typical assumptions of a constant or exponentially declining/increasing SFHs. Another use would be to connect progenitors of galaxies across cosmic time, by examining the typical stellar mass growth of a galaxy observed at a given epoch, as an alternative to using samples matched in number densities (Leja et al. 2013; Behroozi et al. 2013).

6 SUMMARY

We present an analytic model for the growth of the stellar, metal, and gaseous components of galaxies, based on the idea that galaxies grow in equilibrium between inflows, outflows, and star formation, under the assumption of a slowly-evolving gas reservoir. This model contains three baryon cycling parameters that represent preventive feedback, ejective feedback, and wind recycling. We parameterize these as a function of redshift and halo mass, resulting in eight free parameters that we constrain using an MCMC algorithm against three observed scaling relations at $z = 0, 1, 2$: (i) the stellar mass–halo mass relation (essentially equivalent to the stellar mass function); (ii) the mass–metallicity relation; and (iii) the star formation rate–stellar mass relation. The resulting best-fit model fits these observations with an overall reduced $\chi^2 \approx 1.6$. We demonstrate via Bayesian evidence that all eight parameters provide a statistically improved fit over removing any single parameter. We further show that fitting any two of the three above scaling relations results in an acceptable prediction ($\chi^2_{\nu} \lesssim 2$) for the third relation. This indicates that the equilibrium model, with just a small number of physically meaningful parameters, provides a good description of the mean observed evolution of the galaxy population out to $z = 2$.

Given the data we have considered, the best-fit equilibrium model parameters are:

$$\eta = \left(\frac{M_h}{10^{10.98+0.62\sqrt{z}}} \right)^{-1.16}, \quad (11)$$

$$t_{\text{rec}} = 0.52 \times 10^9 \text{ yr} \times (1+z)^{-0.32} \left(\frac{M_h}{10^{12}} \right)^{-0.45}, \quad (12)$$

$$\zeta_{\text{quench}} = \text{MIN} \left[1, \left(\frac{M_h}{M_q} \right)^{-0.49} \right],$$

where $\frac{M_q}{10^{12}M_{\odot}} = (0.96 + 0.48z)$. (13)

Of course, these values may change based on the set of observations one selects to fit, or the exact parameterisations used to describe these quantities. Nonetheless, the above parameters result in a good fit to observed scaling relations out to $z \sim 2$, as well as predictions to higher redshifts that are broadly consistent with observations.

There are numerous broader implications for the success of this model. Perhaps most significant is the simple fact that this model framework based on simple ISM mass balance and rapid and stable gas processing works at all. Considering that most analytically-based galaxy formation models have, for many decades now, all begun with the scenario of star-forming disks forming via cooling flows from hot gas in merging dark matter halos, it is already interesting that one can construct a successful galaxy formation model that does not explicitly refer to halos, cooling, merging, or a disk star formation law. This is not to say that such processes don’t occur or aren’t important, but merely that such processes are not the primary driver for the overall mean evolution of the galaxy population. The equilibrium model instead forwards the idea that it is continual smooth accretion, modulated by continual outflows that sometimes recycle, is the dominant driver. In a sense this model quantifies and formalises the so-called baryon cycle, a term that

has become a fashionable buzzword but had yet to be rigorously defined.

A crucial advantage of this model is its simplicity. With a manageable number of physically well-defined parameters, it becomes more straightforward to obtain physical intuition about how baryon cycling properties impact observable galaxy properties, and vice versa. The small number of parameters also enables a more robust statistical analysis, such as fitting all model parameters simultaneously and being able to examine the Bayesian evidence to formally characterise the necessity of each parameter. The minimal parameter set is in these ways an advantage over SAMs that have far more parameters. However, it is worth noting that SAMs concurrently make predictions for a far larger range of galaxy properties than the model presented here. Hence the equilibrium model should be viewed as a complement to SAMs, or alternatively a new and more simpler framework on which to incorporate all the additional processes that must be included to predict more observed aspects of the galaxy population across cosmic time.

The model presented here only reflects the mean evolution of the galaxy population, therefore it is a zeroth order model for galaxy evolution. Fluctuations around these mean trends are likely to be driven by the lumpy nature of dark matter that cause fluctuations in the inflow rate, including mergers. Inflow fluctuations can give rise to trends such as the SFR dependence of the mass–metallicity relation (e.g. Davé et al. 2011) and stellar mass–gas mass relation (e.g. Rafieferantsoa et al. 2014). Moreover, the lumpiness of inflow can affect the morphology of galaxies, by generating dynamical instabilities within disks that grow bulges either via mergers (Mihos & Hernquist 1996) or more secularly (e.g. Ceverino et al. 2014). These processes that depend on the lumpiness of the accretion can thus be considered to be “first-order” galaxy evolutionary processes, which do not drive the primary zeroth order trends, but nonetheless are crucial to understanding the galaxy population fully. Indeed, the fact that such a simple model so accurately encapsulates zeroth order processes suggests that this portion of the problem is now relatively well understood, and hence at the present time the most interesting studies of galaxy evolution may be quantifying these first-order aspects. A natural extension to the equilibrium model would thus incorporate variations in the inflow rate owing to inflow fluctuations, which can be predicted from halo assembly, but will also need to characterise the timescale to return to equilibrium once perturbed (e.g. the dilution time discussed in Finlator & Davé 2008). We leave this for future work.

The equilibrium model presented here explicitly does not consider galaxy mergers. This is in contrast to SAMs, which are based on merger trees. Recent models and observations have suggested that mergers are sub-dominant for overall galaxy growth (Kereš et al. 2005; Noeske et al. 2007; Rodighiero et al. 2011), and our equilibrium model supports this view. Mergers do likely drive certain rare classes of galaxies such as local starbursts (Sanders & Mirabel 1996), so our current model cannot account for these. Galaxy morphology is likewise not explicitly considered or predicted in our model, and is likely related to mergers. The implication is that these aspects, while interesting, are of secondary importance for the mean growth of stars, gas, and metals in galaxies, though as first-order effects they will provide inter-

esting scatter around the mean scaling relations considered here (Mannucci et al. 2010).

Environment also has important effects on galaxies. While it appears that central galaxy properties are primarily dependent on stellar mass and are (to a few percent level) independent of environment, the properties of satellites can be strongly affected by environment, and even central galaxies that live near larger halos can be impacted (Gabor & Davé 2015). Modeling satellites will thus require extensions of this model that properly capture additional preventive feedback (and perhaps ejective feedback and recycling as well) that are environment-dependent. So far semi-analytic models have had some difficulty reproducing the detailed properties of satellites (e.g. Weinmann et al. 2010; Hearin et al. 2014), so this aspect of galaxy evolution remains far from solved.

Finally, we have not considered gas content in this paper, although it can be straightforwardly incorporated into an equilibrium model (Davé et al. 2012). This would involve introducing another parameter, namely the gas depletion time, but this is in principle not difficult. The depletion time is most directly related to the molecular gas reservoir, but as this is consumed, atomic gas can replenish this. Moreover, the gas reservoir within galaxies is also intimately connected with circum-galactic and intergalactic gas via inflows and outflows. Given these complexities, we have deferred considering gas reservoirs in this model to future work that will discuss all these aspects more cohesively. Nonetheless, with improving observations of gas in various phases across cosmic time, it is clear that such information will provide valuable constraints on the baryon cycling framework of the equilibrium model.

In summary, the equilibrium model recasts analytic galaxy formation within a modern framework based on the simulation-driven paradigm of baryon cycling. Its simplicity and success at matching key galaxy observables with a relatively small number of parameters suggests that it captures the essence of what drives the overall growth of galaxies. Although, the base model has the flexibility to introduce many more free parameters which may further improve the match between the observations and model predictions a bit, the strength of this model is how well it does with so few parameters and also a reduced χ^2 of 1.6 represents a fairly acceptable fit to the data, given all the various systematic uncertainties. We do plan to add more parameters in the future, however, they will be designed to match additional data, such as gas fractions and the scatter around the relations. The MCMC framework presented here represents a base for building models that incorporate a more diverse and sophisticated set of physical processes including inflow fluctuations and mergers, thereby further refining the constraints on the key physical parameters of galaxy growth. Future work will continue to explore and expand upon this basic framework to better understand the origin of an increasingly larger set of galaxy properties.

ACKNOWLEDGEMENTS

The authors acknowledge helpful discussions with P. Behroozi, S. Lilly, Y. Lu, N. Katz, B. Oppenheimer, and J. Zwart. SM and RD acknowledge support from the South

African Research Chairs Initiative and the South African National Research Foundation. This work was supported by the National Science Foundation under grant number AST-0847667, and NASA grant NNX12AH86G.

REFERENCES

- An L., Brooks S., Gelman A., 1998, *Journal of Computational and Graphical Statistics*, 7, 434
- Andrews B. H., Martini P., 2013, *ApJ*, 765, 140
- Asplund M., Grevesse N., Sauval A. J., Scott P., 2009, *Ann. Rev. Astron. & Astrophys.*, 47, 481
- Behroozi P. S., Marchesini D., Wechsler R. H., Muzzin A., Papovich C., Stefanon M., 2013, *ApJL*, 777, L10
- Behroozi P. S., Wechsler R. H., Conroy C., 2013, *ApJ*, 770, 57
- Benson A. J., 2014, *MNRAS*, 444, 2599
- Benson A. J., Pearce F. R., Frenk C. S., Baugh C. M., Jenkins A., 2001, *MNRAS*, 320, 261
- Binney J., 1977, *ApJ*, 215, 483
- Birrer S., Lilly S., Amara A., Paranjape A., Refregier A., 2014, *ApJ*, 793, 12
- Blumenthal G. R., Faber S. M., Primack J. R., Rees M. J., 1984, *Nature*, 311, 517
- Bouché N., et al., 2010, *ApJ*, 718, 1001
- Bower R. G., Benson A. J., Crain R. A., 2012, *MNRAS*, 422, 2816
- Bower R. G., Benson A. J., Malbon R., Helly J. C., Frenk C. S., Baugh C. M., Cole S., Lacey C. G., 2006, *MNRAS*, 370, 645
- Boylan-Kolchin M., Springel V., White S. D. M., Jenkins A., 2010, *MNRAS*, 406, 896
- Brook C. B., Stinson G., Gibson B. K., Roškar R., Wadsley J., Quinn T., 2012, *MNRAS*, 419, 771
- Brooks A. M., Governato F., Booth C. M., Willman B., Gardner J. P., Wadsley J., Stinson G., Quinn T., 2007, *ApJL*, 655, L17
- Ceverino D., Klypin A., Klimek E. S., Trujillo-Gomez S., Churchill C. W., Primack J., Dekel A., 2014, *MNRAS*, 442, 1545
- Chabrier G., 2003, *Publ. Astr. Soc. Pac.*, 115, 763
- Crain R. A., et al., 2009, *MNRAS*, 399, 1773
- Creasey P., Theuns T., Bower R. G., 2015, *MNRAS*, 446, 2125
- Croton D. J., et al., 2006, *MNRAS*, 365, 11
- Daddi E., et al., 2007, *ApJ*, 670, 156
- Dalcanton J. J., Spergel D. N., Summers F. J., 1997, *ApJ*, 482, 659
- Davé R., 2008, *MNRAS*, 385, 147
- Davé R., Finlator K., Oppenheimer B. D., 2006, *MNRAS*, 370, 273
- Davé R., Finlator K., Oppenheimer B. D., 2011, *MNRAS*, 416, 1354
- Davé R., Finlator K., Oppenheimer B. D., 2012, *MNRAS*, 421, 98
- Davé R., Katz N., Oppenheimer B. D., Kollmeier J. A., Weinberg D. H., 2013, *MNRAS*, 434, 2645
- Davé R., Oppenheimer B. D., Finlator K., 2011, *MNRAS*, 415, 11
- Dekel A., et al., 2009, *Nature*, 457, 451
- Dekel A., Mandelker N., 2014, *MNRAS*, 444, 2071
- Duncan K., et al., 2014, *MNRAS*, 444, 2960
- Fall S. M., Efstathiou G., 1980, *MNRAS*, 193, 189
- Faucher-Giguère C.-A., Kereš D., Ma C.-P., 2011, *MNRAS*, 417, 2982
- Faucher-Giguère C.-A., Quataert E., Hopkins P. F., 2013, *MNRAS*, 433, 1970
- Feroz F., Hobson M. P., 2008, *MNRAS*, 384, 449
- Feroz F., Hobson M. P., Bridges M., 2009, *MNRAS*, 398, 1601
- Feroz F., Hobson M. P., Cameron E., Pettitt A. N., 2013, *arXiv:1306.2144*
- Finlator K., Davé R., 2008, *MNRAS*, 385, 2181
- Finlator K., Davé R., Özel F., 2011, *ApJ*, 743, 169
- Gabor J. M., Davé R., 2012, *MNRAS*, 427, 1816
- Gabor J. M., Davé R., 2015, *MNRAS*, 447, 374
- Gnedin N. Y., Kravtsov A. V., 2010, *ApJ*, 714, 287
- Hearin A. P., Watson D. F., van den Bosch F. C., 2014, *arXiv:1404.6524*
- Henriques B., White S., Thomas P., Angulo R., Guo Q., Lemson G., Springel V., Overzier R., 2014, *arXiv:1410.0365*
- Henriques B. M. B., White S. D. M., Thomas P. A., Angulo R. E., Guo Q., Lemson G., Springel V., 2013, *MNRAS*, 431, 3373
- Henry A., Martin C. L., Finlator K., Dressler A., 2013, *ApJ*, 769, 148
- Hopkins P. F., Kereš D., Oñorbe J., Faucher-Giguère C.-A., Quataert E., Murray N., Bullock J. S., 2014, *MNRAS*, 445, 581
- Kauffmann G., White S. D. M., Guiderdoni B., 1993, *MNRAS*, 264, 201
- Kereš D., Katz N., Weinberg D. H., Davé R., 2005, *MNRAS*, 363, 2
- Kewley L. J., Ellison S. L., 2008, *ApJ*, 681, 1183
- Krumholz M. R., Dekel A., 2012, *ApJ*, 753, 16
- Larson D., et al., 2011, *ApJS*, 192, 16
- Leauthaud A., et al., 2012, *ApJ*, 744, 159
- Leitner S. N., Kravtsov A. V., 2011, *ApJ*, 734, 48
- Leja J., van Dokkum P., Franx M., 2013, *ApJ*, 766, 33
- Lewis A., Bridle S., 2002, *Phys. Rev. D*, 66, 103511
- Licquia T. C., Newman J. A., 2015, *ApJ*, 806, 96
- Lilly S. J., Carollo C. M., Pipino A., Renzini A., Peng Y., 2013, *ApJ*, 772, 119
- Lu Y., Mo H. J., Katz N., Weinberg M. D., 2012, *MNRAS*, 421, 1779
- Mannucci F., Cresci G., Maiolino R., Marconi A., Gnerucci A., 2010, *MNRAS*, 408, 2115
- McMillan P. J., 2011, *MNRAS*, 414, 2446
- Mihos J. C., Hernquist L., 1996, *ApJ*, 464, 641
- Mo H. J., Mao S., White S. D. M., 1998, *MNRAS*, 295, 319
- Moster B. P., Naab T., White S. D. M., 2013, *MNRAS*, 428, 3121
- Munshi F., Governato F., Brooks A. M., Christensen C., Shen S., Loebman S., Moster B., Quinn T., Wadsley J., 2013, *ApJ*, 766, 56
- Murray N., Quataert E., Thompson T. A., 2010, *ApJ*, 709, 191
- Narayanan D., Davé R., 2013, *MNRAS*, 436, 2892
- Noeske K. G., et al., 2007, *ApJL*, 660, L43
- Okamoto T., Gao L., Theuns T., 2008, *MNRAS*, 390, 920
- Oppenheimer B. D., Davé R., 2008, *MNRAS*, 387, 577

Oppenheimer B. D., Davé R., Kereš D., Fardal M., Katz N., Kollmeier J. A., Weinberg D. H., 2010, *MNRAS*, 406, 2325

Papovich C., Finkelstein S. L., Ferguson H. C., Lotz J. M., Gialvalisco M., 2011, *MNRAS*, 412, 1123

Peng Y.-j., Maiolino R., 2014, *MNRAS*, 443, 3643

Rafieferantsoa M., Davé R., Anglés-Alcazar D., Katz N., Kollmeier J. A., Oppenheimer B. D., 2014, arXiv:1408.2531

Reddy N. A., Pettini M., Steidel C. C., Shapley A. E., Erb D. K., Law D. R., 2012, *ApJ*, 754, 25

Rees M. J., Ostriker J. P., 1977, *MNRAS*, 179, 541

Rodighiero G., et al., 2011, *ApJL*, 739, L40

Saintonge A., et al., 2013, *ApJ*, 778, 2

Salim S., et al., 2007, *ApJS*, 173, 267

Sanders D. B., Mirabel I. F., 1996, *ARA&A*, 34, 749

Sanders R. L., et al., 2015, *ApJ*, 799, 138

Schaye J., et al., 2015, *MNRAS*, 446, 521

Schreiber C., et al., 2015, *A&A*, 575, A74

Somerville R. S., Davé R., 2015, Submitted to *ARA&A*

Somerville R. S., Hopkins P. F., Cox T. J., Robertson B. E., Hernquist L., 2008, *MNRAS*, 391, 481

Somerville R. S., Primack J. R., 1999, *MNRAS*, 310, 1087

Sparre M., et al., 2015, *MNRAS*, 447, 3548

Speagle J. S., Steinhardt C. L., Capak P. L., Silverman J. D., 2014, *ApJS*, 214, 15

Stark D. P., Schenker M. A., Ellis R., Robertson B., McLure R., Dunlop J., 2013, *ApJ*, 763, 129

Steidel C. C., et al., 2014, *ApJ*, 795, 165

Tacconi L. J., et al., 2013, *ApJ*, 768, 74

Thomas D., Maraston C., Bender R., Mendes de Oliveira C., 2005, *ApJ*, 621, 673

Torrey P., Vogelsberger M., Genel S., Sijacki D., Springel V., Hernquist L., 2014, *MNRAS*, 438, 1985

Tremonti C. A., et al., 2004, *ApJ*, 613, 898

Vogelsberger M., et al., 2014, *Nature*, 509, 177

Weinberg M. D., 2009, arXiv:0911.1777

Weinmann S. M., Kauffmann G., von der Linden A., De Lucia G., 2010, *MNRAS*, 406, 2249

Weinmann S. M., Pasquali A., Oppenheimer B. D., Finlator K., Mendel J. T., Crain R. A., Macciò A. V., 2012, *MNRAS*, 426, 2797

Whitaker K. E., et al., 2014, *ApJ*, 795, 104

White S. D. M., Frenk C. S., 1991, *ApJ*, 379, 52

White S. D. M., Rees M. J., 1978, *MNRAS*, 183, 341

Zahid H. J., Dima G. I., Kudritzki R.-P., Kewley L. J., Geller M. J., Hwang H. S., Silverman J. D., Kashino D., 2014, *ApJ*, 791, 130

APPENDIX: EQUILIBRIUM RELATIONS

Star-forming galaxies closely follow the slowly evolving equilibrium condition between the accretion of cold gas, consumption of gas into stars and outflows. This can be obtained from the basic conservation equation for gas mass (Finlator & Davé 2008; Bouché et al. 2010; Dekel & Mandelker 2014):

$$\dot{M}_{\text{gas}} = \dot{M}_{\text{in}} - \dot{M}_{\star} - \dot{M}_{\text{out}} \quad (\text{A1})$$

where \dot{M}_{in} is the gas accretion rate onto the galaxy’s star-forming region, \dot{M}_{\star} is star formation rate (SFR), and \dot{M}_{out}

is the gas outflow rate. Now, as suggested by hydrodynamic simulations (Finlator & Davé 2008) and analytical studies of galaxy’s self-regulating behavior to a steady state (Bouché et al. 2010; Krumholz & Dekel 2012), along with observations that show that the gas content of galaxies evolves much more slowly than the star formation rate (Tacconi et al. 2013; Saintonge et al. 2013), we make the *equilibrium assumption* that $\dot{M}_{\text{gas}} \simeq 0$ when compared to inflow rates, outflow rates, and SFR (Davé et al. 2012). This yields

$$\dot{M}_{\text{in}} = \dot{M}_{\text{out}} + \dot{M}_{\star} = (1 + \eta)\dot{M}_{\star}, \quad (\text{A2})$$

where $\eta \equiv \dot{M}_{\text{out}}/\dot{M}_{\star}$ is the outflow *mass loading factor*. \dot{M}_{in} is governed by a combination of (i) the gravitational-driven baryonic inflow of dark matter halos (\dot{M}_{grav}) (ii) the gas entering the halo that is prevented from reaching the ISM (\dot{M}_{prev}) and (iii) the gas recycling rate (\dot{M}_{recyc}), associated with the fraction of mass that was ejected earlier in outflows, as follows:

$$\dot{M}_{\text{in}} = \dot{M}_{\text{grav}} - \dot{M}_{\text{prev}} + \dot{M}_{\text{recyc}} = \zeta\dot{M}_{\text{grav}} + \dot{M}_{\text{recyc}} \quad (\text{A3})$$

where, $\zeta \equiv 1 - \dot{M}_{\text{prev}}/\dot{M}_{\text{grav}}$ is the *preventive feedback parameter*. Combining Equation A2 and A3, we get (Davé et al. 2012)

$$\dot{M}_{\star} = \frac{\zeta\dot{M}_{\text{grav}} + \dot{M}_{\text{recyc}}}{1 + \eta} \quad (\text{A4})$$

Here \dot{M}_{grav} is taken from Dekel et al. (2009) as

$$\frac{\dot{M}_{\text{grav}}}{M_h} = 0.47 f_b \left(\frac{M_h}{10^{12} M_{\odot}} \right)^{0.15} \left(\frac{1+z}{3} \right)^{2.25} \text{Gyr}^{-1}. \quad (\text{A5})$$

and ζ can be written as a combination of various contributions, described in Equation 6 of the main text, coming from different sources. For those, we take (following Equation 1 of Okamoto et al. 2008)

$$\zeta_{\text{photo}} = \left[1 + \frac{1}{3} \left(\frac{M_h}{M_{\gamma}} \right)^{-2} \right]^{-1.5} \quad (\text{A6})$$

with M_{γ} given in Figure 3 of Okamoto et al. (2008). For ζ_{winds} , we consider a somewhat arbitrary parameterization to incorporate its qualitative effects (Davé et al. 2012; Narayanan & Davé 2013):

$$\zeta_{\text{winds}} = 1 - e^{-\sqrt{M_h/M_w}}, \quad M_w = 10^{10-0.25z} \quad (\text{A7})$$

and we take ζ_{grav} as derived from hydrodynamic simulations with no outflows (Faucher-Giguère et al. 2011),

$$\zeta_{\text{grav}} = 0.47 \left(\frac{1+z}{4} \right)^{0.38} \left(\frac{M_h}{10^{12} M_{\odot}} \right)^{-0.25}. \quad (\text{A8})$$

To follow \dot{M}_{recyc} in our model, we use the recycling time (t_{rec}) information gained from simulations (Oppenheimer & Davé 2008; Henriques et al. 2013) to track recycling directly. The idea is that, whenever a mass is ejected via outflows, we take that mass (i.e. $\eta \times \text{SFR} \times dt$) in a given time-step dt and put it into a “reservoir” as $M_{\text{recyc}}^{\text{res}}$. Then after some time t_{rec} , the material is re-accreted into the galaxy at a rate $\dot{M}_{\text{recyc}} = M_{\text{recyc}}^{\text{res}}/dt$, where dt is the time-step at time of re-accretion. Note that, here dt is not constant; we adjust it to keep $0.001 < dM_h/M_h < 0.01$, where $dM_h = \dot{M}_h \times dt$.

We also include mass loss from stellar evolution $R(t)$

that goes back into gas, so that the net SFR becomes $(1 - R)\dot{M}_*$, where $R(t)$ for a Chabrier (Chabrier 2003) IMF is well-approximated by (Leitner & Kravtsov 2011; Moster et al. 2013)

$$R(t) = 0.046 \ln \left(\frac{t}{2.76 \times 10^5 \text{ yr}} + 1 \right) \quad (\text{A9})$$

Now, the metal content of galaxies, Z_{ISM} can be derived from the yield times SFR divided by the inflow rate which is yet to be enriched:

$$Z_{\text{ISM}} = \frac{y\dot{M}_*}{\dot{M}_{\text{in}} - \dot{M}_{\text{recyc}}} = \frac{y\dot{M}_*}{\zeta\dot{M}_{\text{grav}}}. \quad (\text{A10})$$

This assumes that the metallicity of re-accreted outflows is similar to that of the galaxy; in detail, the metallicity of a galaxy increases slightly with time, but the outflowing gas is also likely slightly enriched relative to the galaxy at the time of ejection.

The above Equations A4 and A10 are usually referred to as the *equilibrium relations* and the parameters η , ζ and t_{rec} describing these relations are known as *baryon cycling parameters*. Constraining these parameters based on various observations is the main goal of this work.